HUMAN GENETICS

Cellular atlas of the human ovary using morphologically guided spatial transcriptomics and single-cell sequencing

Andrea S. K. Jones[1]†, D. Ford Hannum[2]†, Jordan H. Machlin[1,3], Ansen Tan[1], Qianyi Ma[2,4], Nicole D. Ulrich[4], Yu-chi Shen[5], Maria Ciarelli[1], Vasantha Padmanabhan[4,6,7], Erica E. Marsh[4], Sue Hammoud[3,4,5,8], Jun Z. Li[2,4]*, Ariella Shikanov[1,3,4]*

The reproductive and endocrine functions of the ovary involve spatially defined interactions among specialized cell populations. Despite the ovary's importance in fertility and endocrine health, functional attributes of ovarian cells are largely uncharacterized. Here, we profiled >18,000 genes in 257 regions from the ovaries of two premenopausal donors to examine the functional units in the ovary. We also generated single-cell RNA sequencing data for 21,198 cells from three additional donors and identified four major cell types and four immune cell subtypes. Custom selection of sampling areas revealed distinct gene activities for oocytes, theca, and granulosa cells. These data contributed panels of oocyte-, theca-, and granulosa-specific genes, thus expanding the knowledge of molecular programs driving follicle development. Serial samples around oocytes and across the cortex and medulla uncovered previously unappreciated variation of hormone and extracellular matrix remodeling activities. This combined spatial and single-cell atlas serves as a resource for future studies of rare cells and pathological states in the ovary.

INTRODUCTION

The development, differentiation, and spatial organization of the many cell populations in the human ovary are essential for its reproductive and endocrine functions. The outer ~1.5-mm layer of the organ, the ovarian cortex, contains quiescent primordial follicles, which constitute the follicular reserve, and transitioning and primary follicles and is identified by its dense tissue structure and lesser vasculature (*1*, *2*). The inner part of the organ, the medulla, contains the growing secondary and antral follicles, as well as corpora lutea, presents with a looser extracellular matrix (ECM) structure, and contains more abundant vasculature (*2*, *3*). Both regions are maintained by constant interactions among the stromal, immune, and endothelial cells and other rarer cell types (*4*). The functional unit of the ovary, the ovarian follicle, contains an oocyte in the center, surrounded by specialized somatic cells that secrete hormones and support the many steps of oocyte maturation (*5*). In women of reproductive age, a small portion of quiescent primordial follicles are periodically activated to join the pool of growing follicles (*6*). The growing follicles expand across both the cortex and medulla, each taking on a multilayered three-dimensional architecture containing the oocyte surrounded by cumulus granulosa, and outer layers of mural granulosa, and theca cells, which are separated from the cumulus-oocyte complex by a fluid-filled antrum (*7*). Paracrine cross-talk among the follicular cells and endocrine signals from the hypothalamic-pituitary-ovarian axis work together to trigger ovulation, which produces mature eggs for fertilization (*5*). The cellular diversity of the ovary and the complex spatially defined structures in growing follicles have been difficult to study, largely due to the scarcity of tissue from healthy women of reproductive age, the lack of unbiased functional profiling, and the technical limitations of spatial transcriptomics (ST). Past studies using animal models have identified major classes of ovarian structures and their putative functions using transcriptomics (*4*, *8*). However, human follicle development and the role of nonfollicular cells in this process remain poorly understood, supporting an ST-based characterization of the human ovary to understand follicle development, hormone production, and ovarian aging.

The ovarian cortex is of particular research interest as the home of the follicular reserve and the microenvironment in which follicle activation occurs. In recent years, a few single-cell sequencing studies have reported that the cortex and the medulla contain the same general cell types (*9*), but the two regions are histologically distinct, e.g., having different ECMs tailored to their functions and different gradients of growth factors (*10*). The mechanisms driving follicle activation, either within the follicular structure or from the microenvironment outside the follicles, are poorly understood. Studies of the oocyte compartment of primordial and primary follicles have aimed to identify markers of quiescence and activation, but isolation of oocytes for sequencing may alter their transcriptome or lead to spontaneous activation (*11*, *12*), underscoring the need to collect data from intact tissues to understand what defines these early stages of follicle development. With the recently emerged ST technology, primordial and primary follicles and the surrounding cortical stroma can be sampled with minimal perturbation to uncover cortex-specific gene activities related to early folliculogenesis. Likewise, ST presents a previously unattainable opportunity to profile the gene activities in diverse types of follicles recognized by their morphology and spatial context. Previous studies have reported on the transcriptional profiles of granulosa and theca cells (*9*, *13*), but hypotheses surrounding oocyte-cumulus granulosa cell bidirectional cross-talk and factors influencing the follicular cell phenotypes have not been validated using a spatial approach.

[1]Department of Biomedical Engineering, University of Michigan, Ann Arbor, MI, USA. [2]Department of Computational Medicine and Bioinformatics, University of Michigan, Ann Arbor, MI, USA. [3]Cellular and Molecular Biology Program, University of Michigan, Ann Arbor, MI, USA. [4]Department of Obstetrics and Gynecology, University of Michigan, Ann Arbor, MI, USA. [5]Department of Human Genetics, University of Michigan, Ann Arbor, MI, USA. [6]Department of Pediatrics and Communicable Diseases, University of Michigan, Ann Arbor, MI, USA. [7]Department of Molecular and Integrative Physiology, University of Michigan, Ann Arbor, MI, USA. [8]Department of Urology, University of Michigan, Ann Arbor, MI, USA.
*Corresponding author. Email: junzli@med.umich.edu (J.Z.L.); shikanov@umich.edu (A.S.)
†These authors contributed equally to this work.

In this study, we compiled a functionally targeted ST dataset of the human ovary, composed of 257 regional samples collected using NanoString's GeoMx platform from the ovaries of two reproductive-age, premenopausal donors. We also collected single-cell RNA sequencing (scRNA-seq) data of 21,198 dissociated cells from three additional donors. Using these data, we uncovered transcriptional profiles of primordial and primary oocytes sampled from their native microenvironment, gene signatures of theca and granulosa cells, spatially defined patterns of gene expression across the medulla and cortex, and major stromal and immune cell types of the human ovary. Comparisons between our ST and scRNA-seq datasets confirmed the robustness of the GeoMx platform for sampling specific local regions of small size and distinct function. This integrated analysis led to a comprehensive cell atlas of the healthy reproductive-age human ovary, revealing spatially defined transcriptional patterns and adding to our knowledge on the cellular diversity of this organ.

RESULTS

ST of the human ovary

We used the GeoMx technology to analyze samples from 74 regions of interest (ROIs) in a whole-ovary tissue cross section from a healthy donor, followed by samples from 147 ROIs collected from a second donor. The donors were postpubescent and premenopausal (18 and 27 years old) and had no known reproductive disorders (for complete donor information, see fig. S1A). The ROIs were manually selected on the basis of histological features in different tissue locations to represent known functional units in the ovary (Fig. 1A). The 92 samples in donor 1 represented 14 ROI types, and the sampling in donor 2 was designed to repeat and validate some functional types while extending to additional types based on the analysis of donor 1 data and structures uniquely present in the donor 2 ovary. In all, we analyzed 19 prespecified ROI types (see additional details in fig. S1B and Materials and Methods). Some ROIs produced multiple split samples from the use of antibody-guided collection from subregions within the ROI [called areas of interest (AOIs)], leading to 92 and 165 samples, respectively, from the two donors. A brief description of the ROI types is as follows. Types 1 to 5 represent regions in the ovarian cortex: ovarian surface, cortex, cortex layers, primordial/primary follicles, and primary follicle rings (Fig. 1A). Types 6 to 9 represent regions in the medulla: medulla, follicle-adjacent medulla, medulla cross section, and vascular regions. Types 10 to 14 were sampled from growing ovarian follicles (Fig. 1, B and C): secondary follicle, oocyte from an antral follicle, cumulus granulosa, mural granulosa (referred to from now on as granulosa), and theca (Fig. 1A). Types 15 to 16 were sampled from an ovarian cyst in donor 2: cyst inner layer and cyst outer layer (Fig. 1, A and C). The remaining types were sampled using antibody-guided selection of AOIs enriched for specific cell types: *CD68*$^+$ (type 17) for macrophages, *SMA*$^+$ (type 18) for myofibroblasts and smooth muscle cells, and *PGR*$^+$ (type 19) to identify cells expressing progesterone receptor (PGR) (Fig. 1A).

The ROIs adopted different sizes and shapes and varied by cell counts and sequencing depth. For example, the 74 ROIs from donor 1 covered an average area of ~60,000 μm^2 (range: 7619 to 359,038 μm^2), contained a monolayer of ~400 cells (range: 0 to 2544, based on nuclei counts), and yielded ~806,000 identified transcripts (range: 57,018 to 14,388,977) among the 18,676 unique protein-coding genes analyzed by the GeoMx Human Whole Transcriptome Atlas panel. Likewise, the 147 ROIs from donor 2 covered an average area of ~30,000 μm^2 (range: 576 to 113,204 μm^2), contained an average of 240 cells (range: 0 to 1497), and yielded an average of ~507,000 transcripts (range: 24,863 to 3,404,489).

Cluster analysis of the 74 ROI-based samples in donor 1 and the 165 AOI-based samples in donor 2 (Materials and Methods) revealed six and nine clusters, respectively (Fig. 1, D and E). Notably, although each region contained a mixture of a few hundred cells, their observed clusters mapped to the prerecognized functional types of ROIs from the cortex, medulla, and follicle-enriched sites and were consistent between the two donors (highlighted by color-coded cross-tabulation in Fig. 1F). For example, cluster 1 in donor 1 contained 21 of the 22 ROIs from the cortex (ROI types 1 to 4); clusters 2 and 3 corresponded to the five ROI types (6, 7, 9, 17, and 18) from the cortex to the medulla (Fig. 1F). The ROIs enriched for theca cells and those enriched for cumulus granulosa (type 12) and granulosa cells (type 13) aggregated into well-separated cluster 4 and cluster 5, respectively, in perfect consistency between the two independently sampled follicles (Fig. 1, D and F). The theca- and granulosa-enriched ROIs were spatially adjacent (Fig. 1B, insets); thus, the fact that their expression profiles were distinguishable (as clusters 4 and 5) confirms the location specificity of the technology. Cluster 6 is formed by the single ROI taken from the oocyte of an antral follicle (Fig. 1F), and it was clearly separated in principal component (PC) 3 (fig. S1C). Similarly, in donor 2, clusters 1 and 2 corresponded to the surface regions of the cortex, while clusters 3, 4, 5, and 6 mainly contained ROIs sampled from cortex and medulla to represent local characteristics, such as the ovarian cyst and antibody-targeted subareas enriched for cells expressing cluster of differentiation 68 (CD68) or PGR (Materials and Methods). Donor 2 data confirmed and extended these patterns. For example, ROIs intended to capture theca cells and granulosa cells arose in cluster analysis as distinguishable groups: cluster 7 for theca and cluster 8 for granulosa. Further, nine ROIs in donor 2 had a subarea expressing deleted in azoospermia like (DAZL) analyzed and they stood out as cluster 9, along with two additional oocytes from primordial and primary follicles (Fig. 1, E and F). In short, although each of the locally sampled regions contained a mixture of cells, we were able to reproducibly identify robust gene activity signatures for the oocytes (cluster 6 in donor 1 and cluster 9 in donor 2), the theca cells (clusters 4 and 7 in the two donors), and the granulosa cells (clusters 5 and 8), along with local characteristics in preselected ROI types across cortex and medulla. In the sections below, we will describe these findings in more detail.

Gene expression profile of primordial and primary oocytes

As described above, we profiled an oocyte sample from an antral follicle in donor 1 and it had a distinct gene signature (as cluster 6). Since primordial and primary oocytes are too small to be individually defined ROIs, we relied on an antibody against the oocyte-specific protein DAZL to target the oocyte subarea within each ROI (Materials and Methods; Fig. 2A), leading to nine pairs of DAZL$^+$ and DAZL$^-$ samples. In each ROI, the DAZL$^+$ subarea contains multiple primordial or primary follicles. This allowed us to use the nine DAZL$^+$ samples to represent oocytes in primordial and primary follicles, thus increasing the sample size of oocytes from 1 in donor 1 to 11 in donor 2 (9 DAZL$^+$ plus 2 individually collected primary follicles). The 11 cluster 9 samples, when compared with the other 8 clusters, showed higher expression of previously reported oocyte markers, such as *TUBB8*, *ZP3*, *LHX8*, and *OOSP2* (Fig. 2B) (*1*), and uncovered

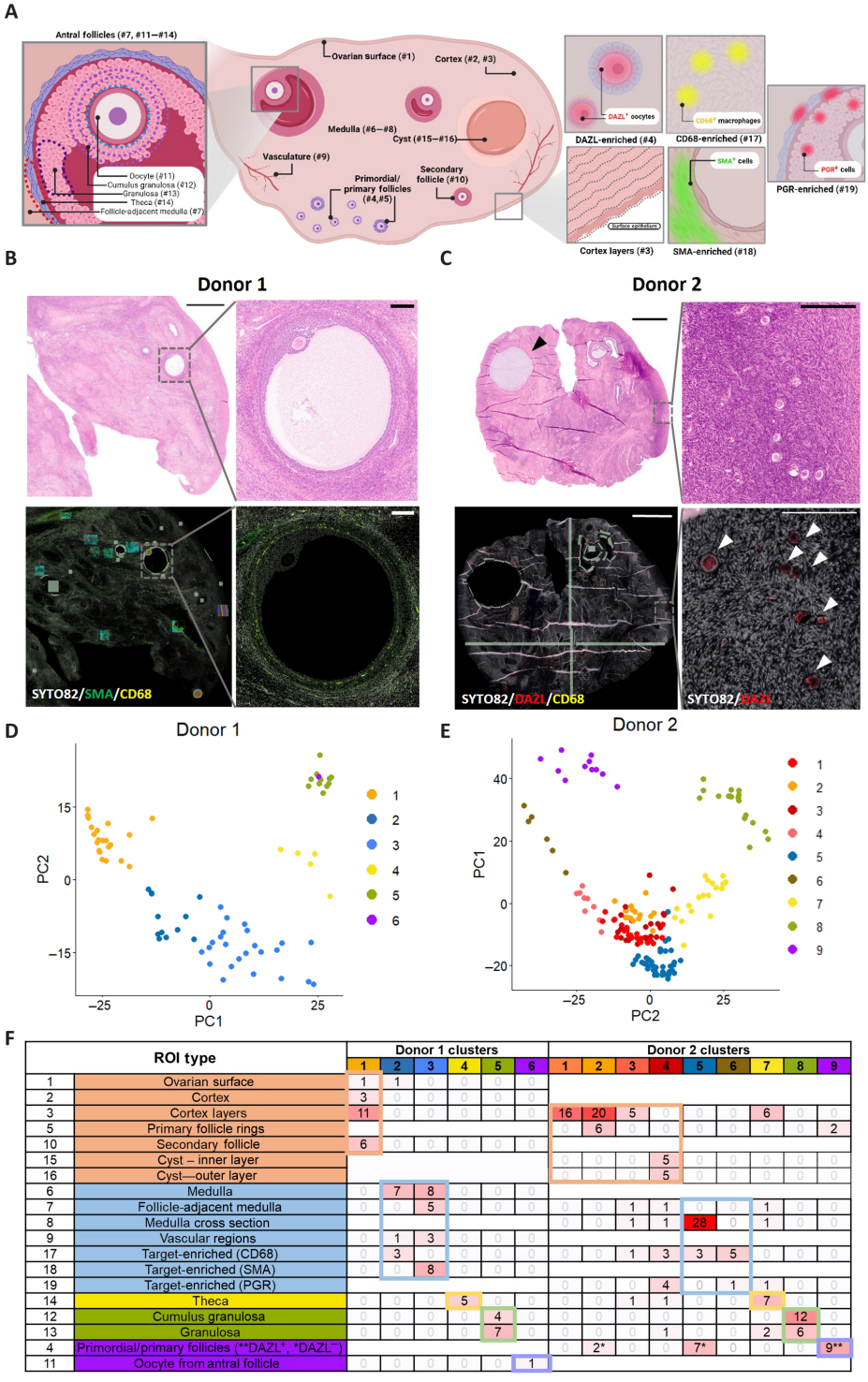

F

	ROI type	Donor 1 clusters						Donor 2 clusters								
		1	2	3	4	5	6	1	2	3	4	5	6	7	8	9
1	Ovarian surface	1	1	0	0	0	0									
2	Cortex	3	0	0	0	0	0									
3	Cortex layers	11	0	0	0	0	0	16	20	5	0	0	0	6	0	0
5	Primary follicle rings							0	6	0	0	0	0	0	0	2
10	Secondary follicle	6	0	0	0	0	0									
15	Cyst – inner layer							0	0	0	5	0	0	0	0	0
16	Cyst—outer layer							0	0	0	5	0	0	0	0	0
6	Medulla	0	7	8	0	0	0									
7	Follicle-adjacent medulla	0	0	5	0	0	0	0	0	1	1	0	0	1	0	0
8	Medulla cross section							0	0	1	1	28	0	1	0	0
9	Vascular regions	0	1	3	0	0	0									
17	Target-enriched (CD68)	0	3	0	0	0	0	0	0	1	3	3	5	0	0	0
18	Target-enriched (SMA)	0	0	8	0	0	0									
19	Target-enriched (PGR)							0	0	0	4	0	1	1	0	0
14	Theca	0	0	0	5	0	0	0	0	1	1	0	0	7	0	0
12	Cumulus granulosa	0	0	0	0	4	0	0	0	0	0	0	0	0	12	0
13	Granulosa	0	0	0	0	7	0	0	0	0	1	0	0	2	6	0
4	Primordial/primary follicles (**DAZL$^+$, *DAZL$^-$)							0	2*	0	0	7*	0	0	0	9**
11	Oocyte from antral follicle	0	0	0	0	0	1									

Fig. 1. ST analysis of the human ovary. (**A**) An illustrated summary of ROI types (all diagrams created with biorender.com). We used the histological image of an adjacent whole-ovary tissue section to select ROIs to represent 19 functional types of local cell communities. (**B**) Hematoxylin and eosin (H&E) (top) and immunofluorescent (IF) images (bottom) of fixed tissue sections from donor 1. Left, whole tissue section. Right, zoomed-in view of an antral follicle. Gray, green, and yellow colors indicate SYTO82, SMA, and CD68 staining signals, respectively. Scale bars, 2.5 mm (left) and 200 μm (right). (**C**) H&E and IF images of fixed tissue sections from donor 2, in the same scale and layout as in (B), except that SMA was not used, and red indicates DAZL signal. Black arrow indicates ovarian cyst; white arrows indicate DAZL expression in primordial/ primary follicles. (**D** and **E**) PC plots (PC1 and PC2) of the 74 ROIs from donor 1 (D) and 165 ROIs from donor 2 (E), colored by the clusters identified. (**F**) Annotation of the observed clusters by their mapping to the predefined ROI types. Sample number cross-tabulation between the 19 ROI types (rows) and the 6 and 9 clusters (columns) in the two donors is shown. The major categories of ROI types and their mapped clusters are highlighted by color: orange, cortex; blue, medulla; yellow, theca; green, granulosa; purple, oocytes. **ROI segments sampled as DAZL$^+$. *ROI segments without DAZL antibody localization.

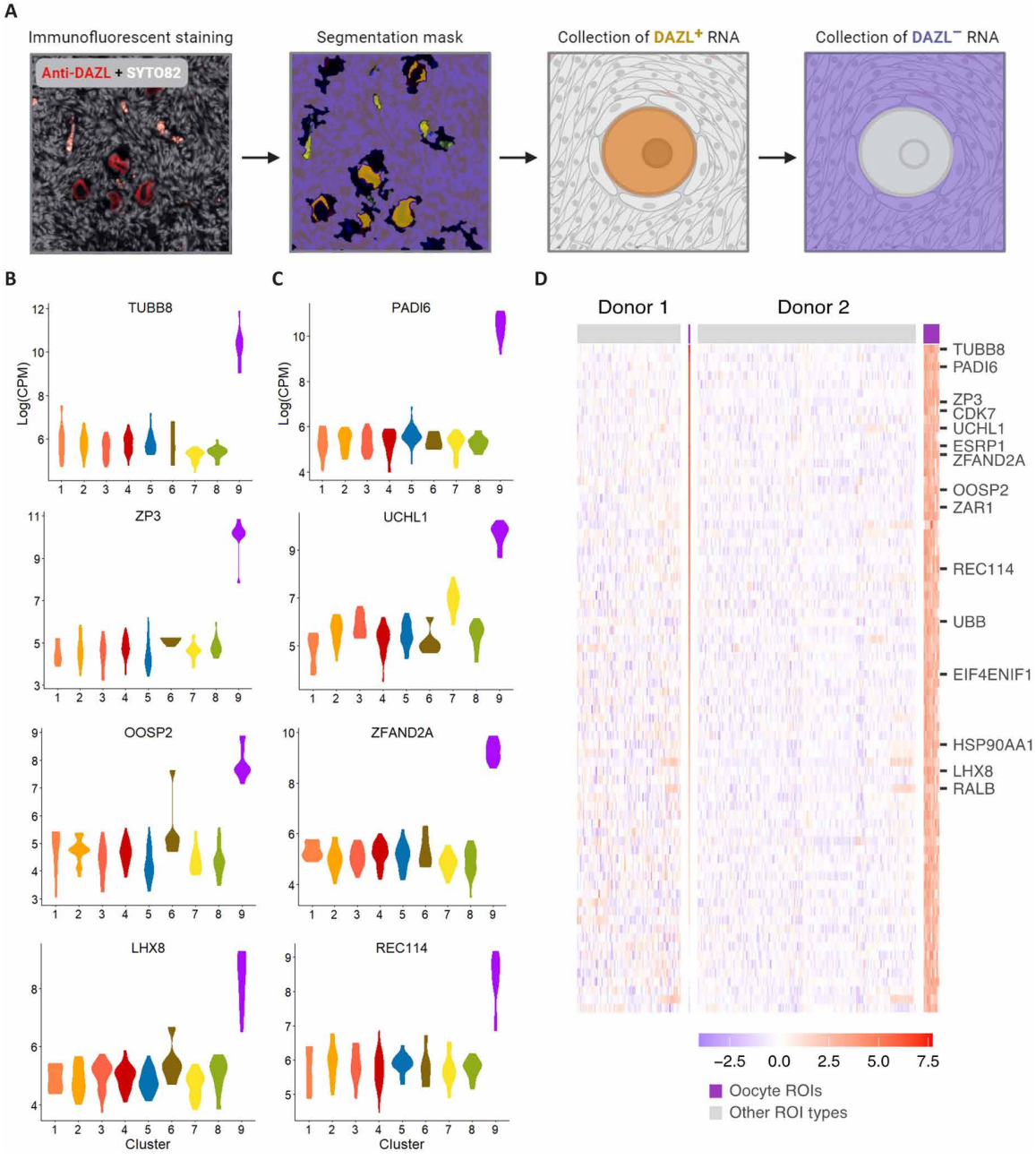

Fig. 2. Transcriptional signature of human oocytes. (**A**) Process of antibody-guided sample collection from subareas of an ROI. In this example, after the sample in DAZL$^+$ area (shown in orange) is collected by photo-activated cleavage, the sample in the remaining areas of the ROI (DAZL$^-$, shown in purple) is collected in a second step, yielding a pair of samples from a single ROI. Created using biorender.com. (**B**) Expression pattern of four previously known canonical oocyte marker genes across the nine clusters in donor 2, where the *y* axis is log(CPM) for all panels. (**C**) Expression of four of previously unreported marker genes, where the *y* axis is log(CPM) for all panels. (**D**) Expression specificity of the 76 oocyte marker genes (in rows) compared across, from left to right, 74 samples from donor 1 ordered by the 6 clusters, and 165 samples from donor 2 ordered by the 9 clusters (data S5). Genes shown in (B) and (C), along with additional genes of interest, are indicated on the heatmap. Per-gene standardization and color scale are explained in Materials and Methods.

previously unreported oocyte markers such as *PADI6*, *UCHL1*, *ZFAND2A*, and *REC114* (Fig. 2C). *PADI6*, which codes for a member of the peptidyl arginine deiminase family, localizes to cytoplasmic lattices in mouse oocytes and has been shown to be essential for early embryonic development (*14*–*16*) but has not previously been reported as oocyte-specific among ovarian cells. Likewise, *UCHL1* codes for a member of the ubiquitin C-terminal hydrolase family of proteins, whose activity contributes to fertilization and embryogenesis in mice (*17*). *REC114* codes for a protein involved in the programmed formation of DNA double-strand breaks during meiosis, but its functional importance for oogenesis has not been extensively characterized in mice or humans (*18*). Last, *ZFAND2A* codes for a protein involved in zinc ion binding

activity and, although not well characterized in humans, has been previously reported as up-regulated in human oocytes (*19*). These studies suggest that these genes may have biological importance for oocyte development, and here, we have shown their oocyte-specific expression compared to all other ROIs. The 11 cluster 9 samples from donor 2 recapitulated the pattern seen in the cluster 6 sample from donor 1. In all, we identified 76 markers for human primordial and primary oocytes (Fig. 2D and data S5), many of which are involved in meiosis (*HSP90A1*, *UBB*, *RALB*, *ESRP1*, *EIF4ENIF1*, *CDK7*, and *ZAR1*). This data file also includes extensive annotations on each gene's possible role in oocyte maturation and folliculogenesis and then orders genes into tiers based on these citations as an established marker, a previously unreported marker with documented biological relevance, a previously unreported marker with little biological relevance, a marker with poor literature annotation, or a marker with relatively poor statistical significance.

Gene signatures of theca and granulosa cells

Among the 74 ROIs in donor 1, the 5 theca and the 11 granulosa ROIs separated into two clusters (clusters 4 and 5, respectively; Fig. 1, D and F). Focused principal components analysis (PCA) of these samples revealed a three-way separation that also distinguished the seven mural granulosa samples from the four cumulus granulosa samples (Fig. 3A). These distinct profiles were reproduced in donor 2 (Fig. 1, E and F), where focused PCA separated the 9, 12, and 11 ROIs enriched for the theca, cumulus granulosa, and granulosa cells into three groups (Fig. 3B), although they were collected from two antral follicles. Differential expression (DE) analysis identified 96 granulosa-specific genes and 45 theca-specific genes (Materials and Methods; Fig. 3C and data S5). The stark contrast in expression of these genes across the two cell types exemplifies their distinct functions. In addition, hundreds of other genes were high in both theca and granulosa cells, but not strongly different between them (data S2).

In donor 1, we also sampled a series of four cumulus granulosa ROIs, each 30 μm wide, corresponding to layers surrounding the oocyte from an antral follicle (Fig. 3D), which was the single sample in cluster 6. We performed a regression analysis across the series of four ordered samples to identify potential gene expression changes in the vicinity of the oocyte. Moving outward from the oocyte, we observed increased expression of Wnt signaling genes (*DDIT3*, *DKK1*, *LEF1*, *TLR3*, and *ZFP91*) (Fig. 3E). Follicle-stimulating hormone (FSH)–mediated down-regulation of this pathway in granulosa cells is important for progesterone production and cumulus cell expansion before ovulation (*20*). Conversely, there was increased expression of genes related to protein kinase A (PKA) signaling (*AKAP12*, *MIF*, *RDX*, and *SPHKAP*) moving inward to the oocyte. PKA signaling in granulosa cells has been well documented in the literature; it modulates FSH-induced granulosa cell differentiation and oocyte maturation as follicle development proceeds (*21*, *22*).

Transcriptional gradient in the ovarian cortex and functional heterogeneity across cortex and medulla

To investigate transcriptome signatures in the outer surface of the ovarian cortex, we selected 11 consecutive regions, each 30 μm thick and 350 μm wide, covering the outer 0.33-mm layer of the donor 1 tissue (Fig. 4A). Notably, although adjacent regions were only 30 μm apart, the gene expression profiles of this linear sample series showed an 11-step, ordered transition (fig. S4A). Linear regression analysis by layer number revealed 313 genes with a significant [false discovery rate (FDR) < 0.05] depth-related expression gradient in the outer cortex (Fig. 4B and data S3). Genes with increasing expression moving inward from the surface epithelium included those involved in hormone signaling (*NR4A1*, *CEBPD*, *STAR*, and *ADAMTS4*), insulin-like growth factor binding protein (IGFBP) signaling (*IGFBP2*, *IGFBP3*, *IGFBP4*, *IGFBP6*, and *IGFBP7*), and ECM remodeling (*VIM*, *COL1A2*, *TIMP1*, *TIMP2*, *MMP2*, *COL8A1*, *COL12A1*, *COL14A1*, *COL16A1*, and *COL18A1*) (Fig. 4B). Both *NR4A1* and *CEBPD* encode transcription factors related to hormone synthesis. *NR4A1* stimulates the expression of *STAR* and other genes involved in androgen production via the PKA pathway (*23*). Luteinizing hormone (LH) stimulates the expression of *CEBPD*, and the resulting transcription factor, CCAAT/enhancer-binding protein δ, has been implicated in LH-triggered events in mature granulosa and theca cells (*24*, *25*). These results show a high-resolution, spatially resolved gradient in the outer cortex, with progressively higher levels of hormone signaling when moving deeper into the cortex layers and more proximal to the growing follicles and the medulla.

To expand this approach when analyzing the donor 2 tissue, we sampled five linear series of consecutive regions: two "medullary series" (M1 and M2) traversing the short and long axes of the tissue section, and three "cortex series" (C1 to C3) covering 1.5 mm of the cortex (Fig. 4C). Each series contained 15 or 16 consecutive straight-line samples. The cortex series started at the surface epithelium from three sides of the tissue section, with sample width of 150 μm and depth of 100 μm. The medulla series had the same width (150 μm) and depth of 500 μm, and they connected with the cortex series at the end. In the overall clustering of all donor 2 samples, most of the ROIs from the three cortex series fell into clusters 1 ($n = 16$) and 2 ($n = 20$), which are cortex sample clusters, while a few others were mixed into other clusters, i.e., five in cluster 4, which "tracks" toward cluster 6—the $CD68^+$ samples (Fig. 1E), and six in cluster 7—mainly containing theca samples (Fig. 1F). The medullary series were more homogeneous, with 28 of the 31 samples forming cluster 5, which also contained seven of the nine $DAZL^-$ samples surrounding primordial and primary follicles (Fig. 1F). Focused PCA of the five series and the nine $DAZL^-$ samples showed these patterns in more detail (PC1 to PC3 in Fig. 4D and PC1 and PC2 in fig. S4B). Samples in each of the three cortex series covered a wide PC1 to PC3 space, yet they did not follow a linear gradient and did not clearly replicate each other (fig. S4C), reflecting diverse functional characteristics being sampled. For example, the cortex series drove clusters 1 and 2, yet they came near cluster 3 (Fig. 1E), which had all 10 samples for ovarian cyst, along with 4 of 5 of PGR^+ and 3 of 12 $CD68^+$ samples (Fig. 1F). Other cortex samples may have been near blood vessels, regions of atresia, or medulla samples with high CD68 expression. In general, the three cortex and the two medulla series are separable in PC3 (Fig. 4D), with one of the cortex series resembling the two medullary series in PC1 (fig. S4B), while the nine $DAZL^-$ samples, which were from cortex regions dense with primordial and primary follicles (Fig. 2A), appeared to "bridge" the space between the cortex series and the medullary series (Fig. 4D). In sum, while the 11-sample series in the outer cortex of donor 1 showed a clean, linear gradient using 30-μm layers, the three cortex series of 1.5-mm tissue depth using 100-μm layers in donor 2 revealed more heterogeneity, and the two medulla series showed a relatively homogeneous profile (cluster 5) for samples in the interior of the ovary.

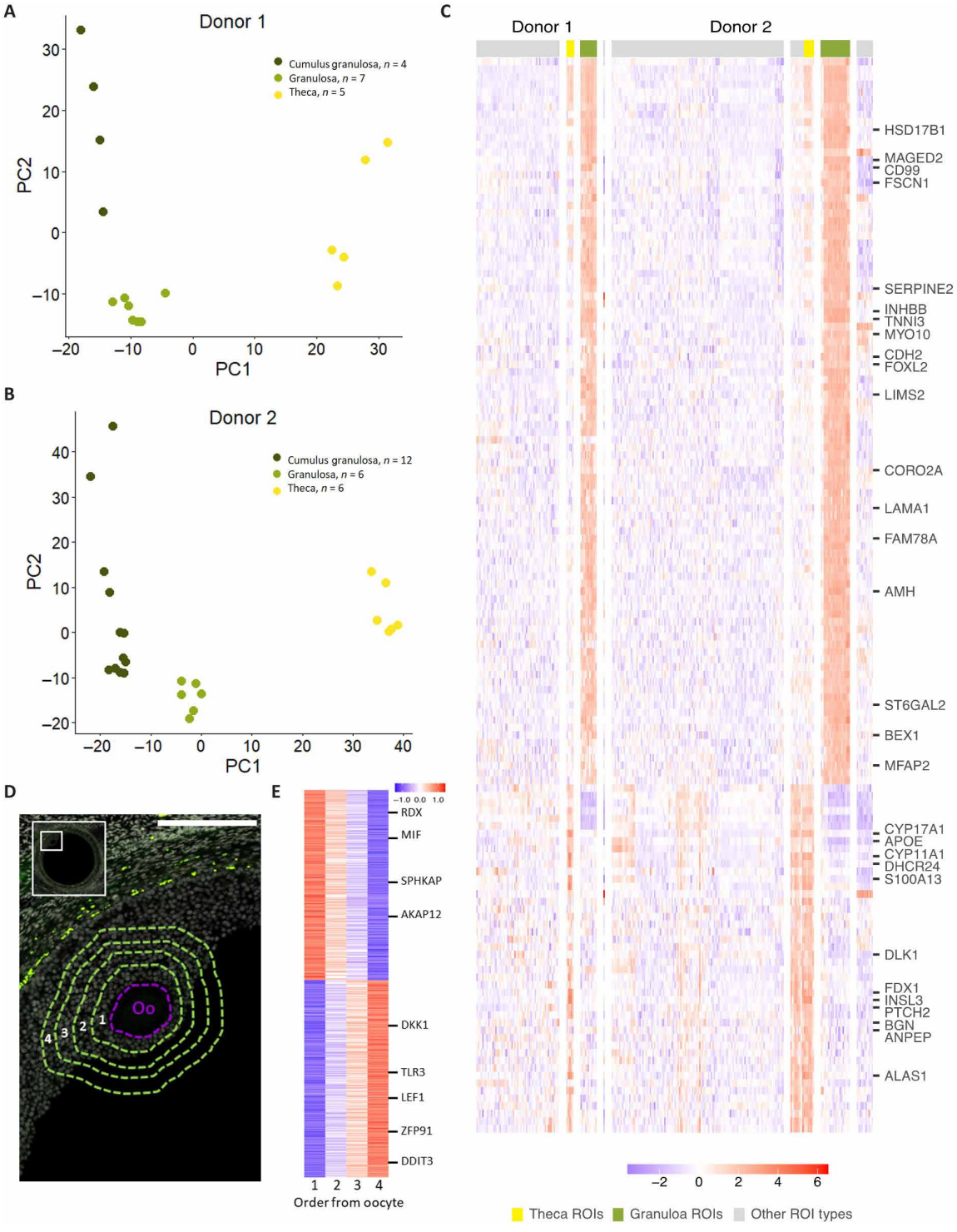

Fig. 3. Robust signatures of granulosa and theca cells. (**A**) Focused PCA of the 5 theca-enriched ROIs and 11 granulosa-enriched ROIs from donor 1, showing their separation into two clusters. (**B**) Similar PC plot for 6 theca and 18 granulosa ROI samples from donor 2. (**C**) Expression specificity of the 94 granulosa cell maker genes (top) and the 45 theca cell marker genes (bottom), compared across the 74 and 165 samples from the two donors, ordered by clusters in the same way as in Fig. 2D (data S5). Color scale explained in Materials and Methods. (**D**) Four concentric ring-shaped ROIs, for cumulus granulosa regions surrounding the oocyte in an antral follicle from donor 1 (scale bar, 100 μm). Purple denotes the oocyte in an antral follicle ("Oo"), while green denotes the four concentric rings of cumulus granulosa cells. (**E**) Regression analysis over the ordered series of four ROIs in (D) identified 1407 DE genes ($P < 0.05$), shown as a heatmap of genes (in rows) across the four samples. Color scale explained in Materials and Methods.

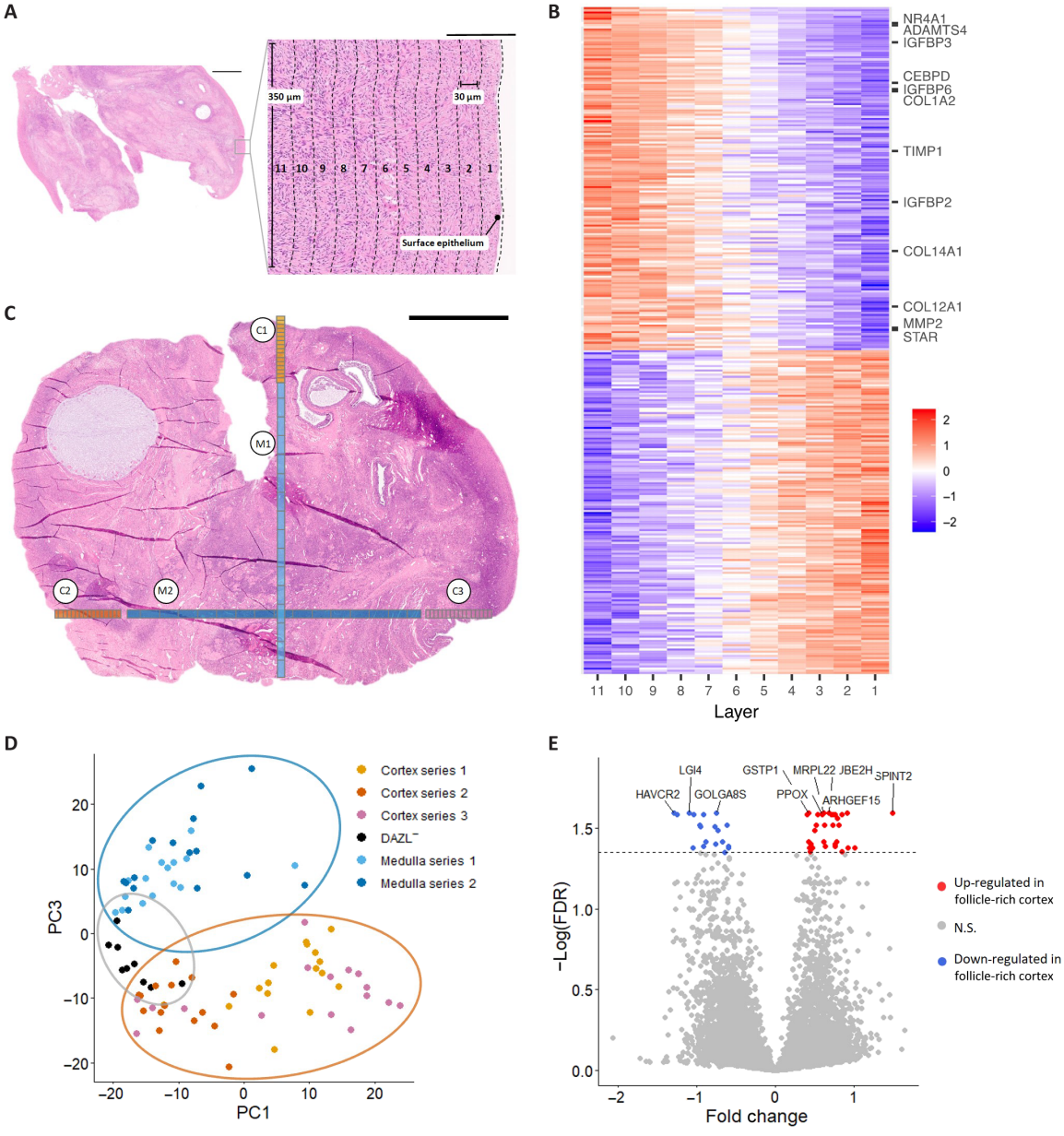

Fig. 4. Transcriptional heterogeneity across cortex and medulla areas. (**A**) In donor 1, a series of 11 consecutive tissue layers were sampled at the surface of the cortex, each with 30-µm depth and 350-µm width (scale bar, 2.5 mm; scale bar for inset, 100 µm). H&E image is shown. (**B**) Linear regression analysis over the 11 ordered samples identified 313 differentially expressed genes ($P < 0.05$), shown as a heatmap, with notable genes indicated to the right. Color scale explained in Materials and Methods. (**C**) Five straight-line series of 15 to 16 consecutive samples for donor 2, three for cortex regions (three warm colors) and two traversing the medulla (two blue colors), indicated on the H&E image (scale bar, 2.5 mm). (**D**) PC1 to PC3 plots of the three cortex and two medulla series, each with 15 to 16 samples, plus the nine DAZL$^-$ subareas near the follicles. The six series are shown in different colors. (**E**) Comparison between the nine DAZL$^-$ near-follicle ROIs and the three surface-most cortex ROIs, one from each of the three cortex series, identified genes that are significantly (FDR < 0.05) higher (red, $n = 33$) and lower (blue, $n = 21$) in follicle-rich cortex versus cortex without follicles. The "volcano plot" of fold change (*x* axis) and negative logged FDR (*y* axis) is shown.

We performed a series of DE analyses among these clusters to elucidate their functional characteristics (Materials and Methods). The medulla samples (cluster 5), when compared to cortex samples (clusters 1 to 3), showed higher expression of *WFIKKN2*, *GSTM5*, and *IGFBP5* and enrichment for terms related to protein targeting to the endoplasmic reticulum and RNA translation (data S3 and S4, "DE11"). Conversely, the cortex samples showed higher expression of *APOC1*, *DNAI3*, *CYP17A1*, and *DHCR24* (data S3 and S4, DE11). Within the cortex samples, clusters 1 to 4 represented several characteristics. Cluster 4 was connected with CD68$^+$ samples in cluster 6 (Fig. 1E), suggesting that they carry local inflammation signatures. Cluster 3 (dark red in Fig. 1E) contained all 10 cyst samples and likely represents signatures of dysregulated follicle development or regressing follicles. Cluster 2 contained all six "rings" around the

primary follicles, while cluster 1 (bright red), consisting entirely of 16 samples from the cortex series without drawing any other ROI types, was closest to the medulla profile in cluster 5 (Fig. 1F). In data S3 and S4, we compared clusters 1/3 against cluster 2 (DE8) and cluster 3 against cluster 1 (DE7) for increasingly finer distinctions among different types of cortex regions. For example, clusters 1/3 showed higher expression than cluster 2 of *DHCR24*, *CYP17A1*, *APOC1*, and *GSTA1* and enrichment for gene ontology terms related to cellular response to steroid synthesis and cholesterol metabolism. Conversely, cluster 2 showed higher expression of *WFIKKN2*, *GSTM5*, and *IGFBP5* and enrichment for terms related to protein targeting to the endoplasmic reticulum and RNA translation. Similar DE results for the cortex and medulla clusters for donor 1 (Fig. 1D) are also included in data S3 and S4.

We also compared transcriptional profiles of (i) cortex regions dense with follicles: the nine $DAZL^-$ samples against (ii) the three surface-most ROIs, which contained no follicles, one from each of the three cortex series. Both groups are composed of ovarian cortical stromal cells but differ in their proximity to ovarian follicles: follicle-rich versus follicle-null. DE analysis revealed 38 genes with significantly ($P < 0.05$) higher expression in the follicle-rich cortex, including *SPINT2* and *ARHGEF15*, and 26 genes with significantly ($P < 0.05$) lower expression (Fig. 4E). *SPINT2* codes for the protein HAI2 and was highly expressed in granulosa cells previously (*5*). HAI2 is a key inhibitor in the hepatocyte growth factor (HGF) signaling pathway, which has been shown to modulate the remodeling of the ovarian surface epithelium and cortex after the cyclic disruption caused by ovulation (*26*). *ARHGEF15* was recently identified in Sertoli cells and shown to be essential to spermatogenesis (*27*). The identification of these genes in follicle-rich cortex may aid the understanding of how the cortex maintains a microenvironment conducive to follicle development, from quiescence to activation.

scRNA-seq of three ovaries from reproductive-age women

Other than the two samples analyzed for ST, we collected scRNA-seq data from three additional donors (donors 3 to 5, ages 28, 37, and 31; fig. S1A). In all, we measured 37,047 cells, of which 21,198 passed quality filtering (Materials and Methods), with an average of 6950 unique transcripts and 2066 detected genes per cell. Clustering analysis for each donor consistently revealed four major cell types (donor 5 in Fig. 5A, donors 3 and 4 in fig. S5, A and B): stromal cells, immune cells (appearing as two clusters in the joint analyses of all cells and as subclusters in Fig. 5B), endothelial cells, and pericytes, and they were identified by known marker genes (Fig. 5C). Endothelial cells showed high expression of their canonical markers *VWF*, *PECAM1*, *CD34*, and *CLDN5* (*9*, *13*), as well as *NOTCH4*, which is typically confined to arterial and sprouting endothelial cells (*28*). Pericytes were identified by their characteristic expression of *RGS5*, *NOTCH3*, *ACTA2*, and *MUSTN1* (Fig. 5, C and D). Pericytes in our data showed high expression of *PDGFRB*, which has been reported in other organ systems for platelet-derived growth factor (PDGF) signaling between pericytes and endothelial cells, and it is also essential to proper theca cell development and steroidogenesis (*29*).

Focused clustering of the immune cells from all three donors revealed four immune cell subtypes (Fig. 5B), which were annotated as T cells (*CD3D*, *CD3G*, and *IL7R*) (*9*, *13*), natural killer (NK) cells (*KLRD1*, *TRCD*, and *GNLY*) (*24*, *30*), macrophages (*CD68*, *CD14*, and *FOLR2*) (*9*, *13*), and mast cells (*KIT*, *TPSB2*, and *TPSAB1*) (*31*, *32*) (Fig. 5C). Additional genes that are specific for the three major cell types and the four immune cell subtypes (Fig. 5D and data S2) add to the expanding cell atlas for the healthy human ovary.

Stromal cells had by far the largest number, reflecting the dominance of this cell population in the ovary. As a group, they were characterized by mesenchymal cell markers *DCN* and *PDGFRA* and the more recently reported ovarian stromal cell markers *APOE*, *LUM*, *ARX*, and *FHL2* (Fig. 5D) (*9*, *13*). Focused analyses of the stromal cells did not reveal clear subtypes (see Materials and Methods for details). Since the spatial analyses generated robust gene lists for the oocyte, theca cells, and granulosa cells, we used these marker panels to score each stromal cell for its chance to be a theca-like or granulosa-like stromal cell and, in even rarer cases, be an oocyte. After carefully selecting the subset of stromal cells with high sequencing depth and using genes with high detection rate, we projected the stromal cells for each of the three donors separately and then asked whether the theca, granulosa, and oocyte scores tend to aggregate in some regions of the projection. Of the multiple scoring algorithms examined, a few showed that some stromal cells scored high for the theca gene panel, and many of them also scored high for the granulosa panel, although to a lesser degree (fig. S5B). Nonetheless, these stromal cells did not clearly separate as a distinct subtype. The oocyte scores did not reveal any clear-cut rare population to be potential oocytes (fig. S5B). This is not unexpected, as oocytes are extremely rare in the dissociated cells from the tissue and there is a ~30-μm size limit in the cell-capturing apparatus. In sum, stromal cells were the most abundant in our data and they appeared homogeneous, with some evidence for a rare subset to be theca-like.

Comparisons with previous scRNA-seq studies

We compared our marker gene lists from spatial data and the major cell types from scRNA-seq with two previously published scRNA-seq data for human ovary. Fan *et al.* (*13*) identified five major cell clusters, including a mixed theca/stromal (Th/S) population and a granulosa cluster (G). We calculated centroid-centroid cross-correlation values between each of the five clusters in that study and each of our six ROI clusters in donor 1 and nine ROI clusters in donor 2 and observed the expected high correlation between Fan *et al.*'s (*13*) granulosa cluster and our granulosa ROI clusters (fig. S6A). The correlation with the Th/S cluster was high for our theca clusters, but also high for our cortex and medulla ROIs. The reduced specificity is likely because Th/S did not distinguish between the theca and stromal cells. Next, we examined the expression pattern of our three lists of marker genes in Fan *et al.*'s (*13*) cluster centroids. As expected, our granulosa markers show high expression in the G cluster, while our theca markers were moderately high in Th/S (fig. S6B).

Wagner *et al.* (*9*) identified six major cell types, including a granulosa cluster and an oocyte cluster. Centroid-centroid correlation values revealed their high correspondence with our granulosa and oocyte ROI clusters (fig. S6C). Likewise, expression patterns of our marker genes showed high specificity in Wagner *et al.*'s (*9*) granulosa and oocyte cluster centroids (fig. S6D).

To compare with our scRNA-seq data, we calculated centroid-centroid correlation values between our four major cell types with Fan *et al.*'s (*13*) five cell types (fig. S6E) and with Wagner *et al.*'s (*9*) six cell types (fig. S6F), and observed that the stromal, immune cells, and endothelial cells match across all three studies, while pericytes in Wagner *et al.* (*9*) and in our study match the smooth muscle cells in the Fan *et al.* (*13*) study. Last, we regenerated the *t*-distributed stochastic neighbor embedding (*t*-SNE) projection

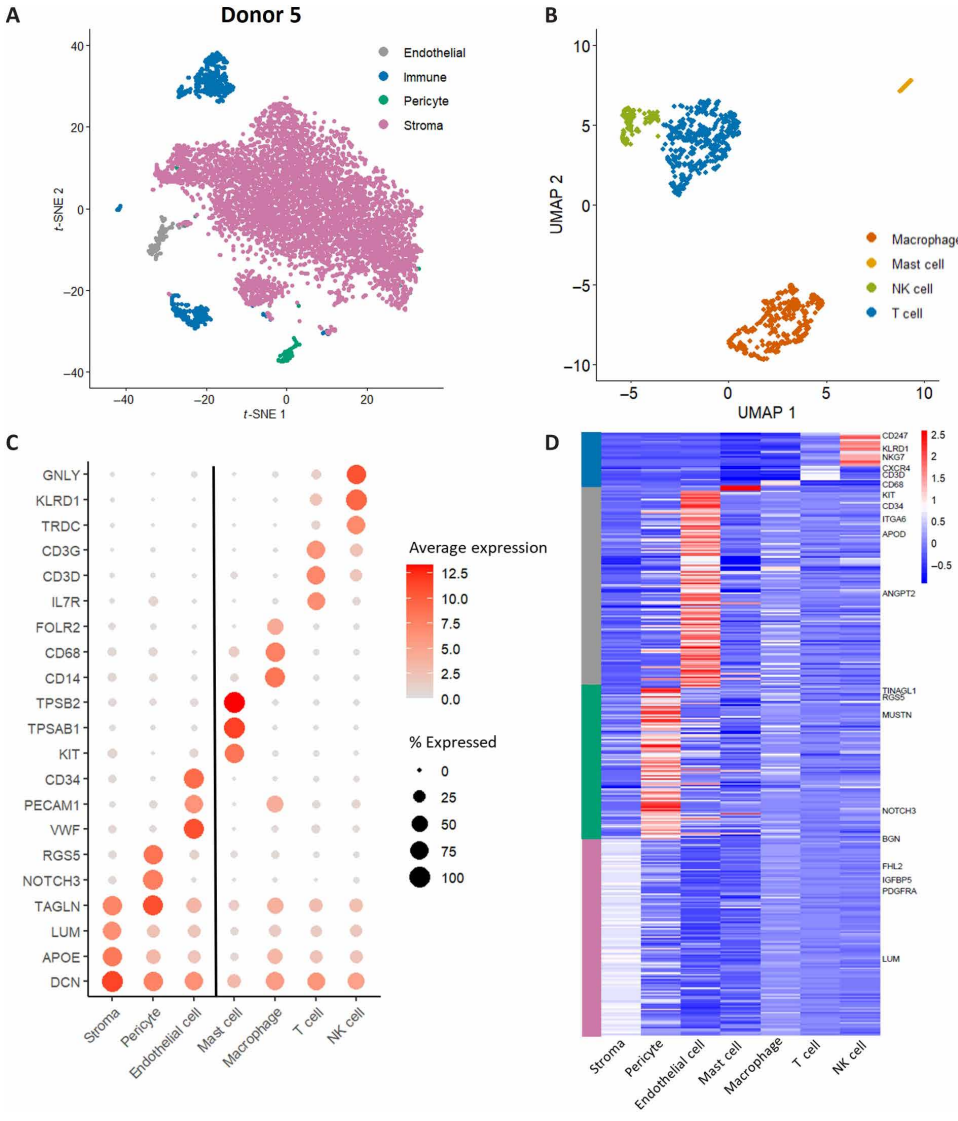

Fig. 5. Cell types in the human ovary identified by scRNA-seq analysis. (**A**) *t*-SNE projection of 6339 cells from donor 5 colored by the four major cell types identified. (**B**) UMAP projection of immune cells ($n = 863$ from three donors) colored by the four immune cell subtypes identified. (**C**) Known marker genes used to annotate the three major cell types and four immune cell subtypes. Color indicates expression level, while symbol size indicates detection rate. (**D**) Centroid data for marker genes for the three major cell types and four immune cell subtypes. Number of genes displayed: stroma, 119; pericyte, 92; endothelial, 120; mast cell, 3; macrophage, 3; T cell, 9; NK cell, 19 (data S6 and S7). Additional literature-based marker genes are indicated on the right. Color scale explained in Materials and Methods.

of Fan *et al.*'s (*13*) single cells and calculated, for each cell, a "theca score" using our theca markers (Materials and Methods). In their Th/S cluster, there seemed to be a subcluster with high theca scores (fig. S6G), suggesting the existence of a subpopulation of theca-like cells that could have been revealed with the theca markers from our spatial data. We then calculated the correlation values between our four immune cell subtypes and Fan *et al.*'s (*13*) finer subtypes (fig. S6H). While the mast cells we identified did not have a clear correspondence, our NK, T cell, and macrophage clusters correspond to their immune subtypes 1, 2, and 3, respectively. In sum, the comparisons with the two previous studies strengthened the validity of the three marker gene lists from our spatial data and verified the annotation of four major cell types in our scRNA-seq data.

DISCUSSION

In this study, we systematically analyzed the spatial and cellular heterogeneity of the human ovary using samples from donors without a history of cancer, previous androgen therapy, or known diseases that affect ovarian function. In contrast to biopsies taken during surgery, the whole cadaveric ovaries we used allowed us to select functional regions throughout the tissue for spatial analyses and to isolate single cells from both cortex and medulla. In the past, studies of ovarian function have faced at least three challenges. First, dissociated cells are dominated by the most abundant cell type: the stromal cells, while the functionally most important cells—those of the follicles—are exceedingly rare, even in the ovarian cortex. Second, cell sorting efforts to enrich for oocytes, theca cells, or granulosa cells, and attempts to visualize them in the intact tissue, relied on a few known

markers, without characterizing the activities and spatial patterns of other genes in an unbiased fashion. Third, some of the earliest and most popular ST technologies are only able to analyze coarse regions at prespecified grid points (e.g., Visium's spots are 55 μm in diameter, with a spot-to-spot distance of 100 μm), yet the functional units of the human ovary, especially the primordial and primary follicles, are in the size range of 20 to 50 μm. We addressed these challenges by adopting NanoString's GeoMx technology, which is unbiased (i.e., it profiles nearly all coding genes) and allows focal analyses of individually selected tissue areas, or even subareas targeted by specific antibodies. In all, we analyzed 92 samples from 74 ROIs in one donor, followed by 165 samples from 147 ROIs from a second donor, covering a wide variety of functional regions across the whole ovary. This strategy allowed us to avoid spending most of the resources on collecting data from the stromal cells and yielded local transcriptomic profiles around both primordial/primary and antral follicles. We then complemented this powerful series of spatial data with scRNA-seq, identifying major cell types such as stromal cells, pericytes, endothelial cells, and four subtypes of immune cells.

For oocytes, we profiled an oocyte from an antral follicle in donor 1 and 11 samples in donor 2 representing primordial and primary oocytes. These samples cluster well among themselves and are clearly enriched for canonical oocyte markers (Fig. 2B), confirming that the GeoMx technology, including the use of anti-DAZL antibody–guided sample collection, can profile oocytes in tissue sections. These data led to a list of 76 oocyte-specific genes, including those related to meiosis (*REC114*) and embryonic development (*PADI6* and *UCHL1*) (Fig. 2, C and D). As a community resource, this list provides many more gene candidates than before for developing reagents to study oocytes of different stages.

Similarly, we took advantage of the custom ROI selection capability of GeoMx to identify dozens of genes specific for theca and granulosa cells (Fig. 3C). These two cell types reside in adjacent areas within developing follicles and are difficult to dissect into separate samples. Thus, the fact that they arose in our data as distinct clusters (Fig. 1, D and E) and were stably reproduced across follicles and across donors confirms the functional identity of these cells as well as the location specificity of the technology. The list of theca-specific genes included canonical theca cell markers *CYP17A1*, *PTCH2*, *APOE*, *DHCR24*, *INSL3*, *BGN*, and *CYP11A1* (*33*, *34*) and the more recently reported *ANPEP* (*35*) (data S5), as well as those not previously reported for theca, but having notable biological relevance, such as *S100A13*, *ALAS1*, *FDX1*, and *DLK1* (data S5). *S100A13* codes for a calcium-binding protein and has been reported as enriched in Leydig cells in a comparison of cell lines from different organ systems (*36*), but its biological importance in Leydig cells or their ovarian counterpart, theca cells, has yet to be elucidated (*36*). Notably, the list included *FDX1* and *ALAS1*, which play important roles in cholesterol acquisition and heme biosynthesis, respectively, both of which are important for the conversion of cholesterol into androgens by the P50 steroidogenic enzymes in theca cells (*37*, *38*). Last, *DLK1* codes for a transmembrane protein that has been implicated in growth hormone signaling, which is essential for theca cell differentiation (*21*, *39*).

Likewise, the list of granulosa-specific genes included canonical marker genes *HSD17B1*, *INHBB*, *FOXL2*, and *AMH* and the recently reported *TNNI3*, *MAGED2*, *CD99*, *SERPINE2*, *CDH2*, and *BEX1* (*9*, *13*), along with many histone protein-coding genes (data S5), which have not been reported for granulosa cells. However, numerous studies have suggested that proliferating granulosa cells undergo large-scale epigenetic change during late folliculogenesis, partly driven by gonadotrophins such FSH (*40*–*43*). The list also included genes involved in granulosa cell–oocyte signaling, such as the transzonal projection–related genes *FSCN1* and *MYO10*, and the tetraspanin protein gene *TSPAN7*, which is involved in extracellular vesicle–mediated signaling between granulosa cells and the oocyte (*44*, *45*). The list confirmed many of the genes previously reported as upregulated in granulosa cells in RNA-based comparisons: *LIMS2*, *CORO2A*, *LAMA1*, *FAM78A*, *ST6GAL2*, and *MFAP2* (*20*, *46*, *47*). Further analyses revealed the finer distinction between cumulus granulosa and the other granulosa layers (Fig. 3, A and B), and a gene activity gradient across concentric layers of cumulus granulosa around the oocyte in an antral follicle (Fig. 3, D and E). More detailed analyses of such gradients are needed to examine the long-standing hypothesis of bidirectional cross-talk between the oocyte and the cumulus cells during follicle development (*1*–*3*).

We collected nine sample pairs in cortex regions dense with primordial and primary follicles, where the $DAZL^+$ sample of the pair corresponds to the oocyte, while the $DAZL^-$ sample represents cortex cells surrounding the follicles (Fig. 2A). The $DAZL^-$, "follicle-rich" cortex regions gave us the opportunity to compare them with other "follicle-null" outer cortex samples (fig. S4D) to identify genes that may be involved in the development of primordial and primary follicles through the emergence of theca and granulosa cells, and through their spatial organization around the maturing oocyte. This analysis highlighted genes related to steroidogenesis (*ARHGEF15* and *GSTP1*) and tissue remodeling (*SPINT2*) (Fig. 4E), and they need further validation to understand how the ovarian stroma influences follicle quiescence and early development.

Since it is impractical to cover the entire tissue section with ROIs, we systematically profiled serial samples across several cortex and medulla regions. In donor 1, we used 11 consecutive samples, at 30-μm-thick increments, to study the outer cortex, and observed a graded change in genes related to hormone signaling (*NR4A1*, *STAR*, and *ADAMTS4*) and ECM remodeling (*VIM* and *COL8/12/14/16/18*) (Fig. 4, A and B). Using a similar approach in donor 2, we sampled three straight-line, linear series, with 100-μm increments, to span the full 1.5-mm depth of the cortex, and two series of medulla samples to traverse the entire long and short axis of the tissue. These cortex and medulla series did not show clean gradients (Fig. 4C); rather, they confirmed the medulla-cortex difference (Fig. 4D) we had seen in donor 1 and revealed transcriptional variation across the surface and the interior of the ovary. For example, the cortex series, from the very surface to 1.5 mm deep, did not always "start" in the same transcriptomic state (fig. S4D), nor end in similar profiles; rather, the 15 or 16 samples in each series "visited" multiple functional characteristics (fig. S4C) that may correspond to areas of atresia, vasculature, or immune activity, which were not evident at the time of sample selection. Nonetheless, some broad patterns did emerge: The two medulla series are similar and clustered away from the three cortex series (Fig. 4D), and one of the three cortex series is more medulla-like (fig. S4B). Within the cortex samples, we found a steroidogenic profile in clusters 1 and 3, with high expression of *DHCR24*, *CYP17A1*, and *GSTA1*, while cluster 2 showed high expression of *WFIKKN2*, *GSTM5*, and *IGFBP5* (DE8 in data S3). Future studies will need denser sampling and more detailed local phenotyping to fully understand the functional changes that accompany follicle development in various regions of the medulla and cortex.

Our scRNA-seq data revealed four major cell types, which are mostly in agreement with those reported by two previous studies. In one, Fan *et al.* (*13*) analyzed 20,676 cells isolated from antral follicles from five donors undergoing fertility preservation before anticancer treatment and identified five major types: Th/S, granulosa (G), immune (Imm), endothelial (E), or smooth muscle (SmMusc) (*13*). On the basis of comparative analyses in fig. S6 (A and B) and the top marker genes reported for each cluster, their Th/S clusters likely matched our stromal cells (*TCF21*, *DCN*, *LUM*, *IGFBP5*, and *APOE*). Three of their immune clusters corresponded to our NK cells (*GNLY*, *KLRD1*, and *CTSW*), T cells (*CD3D* and *CXCR4*), and macrophages (fig. S6H), respectively. Their endothelial clusters mapped to our endothelial cells (*VWF*, *A2M*, and *CLDN5*), while their smooth muscle clusters corresponded to our pericytes (*RGS5*, *ACTA2*, and *TAGLN*), as also seen in fig. S6C. We did not enrich for rare follicular cells through follicle resection or marker-guided enrichment, and as a result, we did not identify granulosa and theca cell clusters. However, the granulosa- and theca-enriched ROIs from our spatial analysis emerged as distinct clusters, and they correlated specifically with the Th/S and granulosa clusters, respectively, from the Fan *et al.* (*13*) study. In a second study, Wagner *et al.* (*9*) profiled 12,160 cells isolated from the ovarian cortex of four donors undergoing caesarean section or gender reassignment surgery (*9*) and identified five types of somatic cells: immune, endothelial, granulosa, stromal, and smooth muscle cells. They reported high expression of *PDGFRA*, *DCN*, *COL1A1*, and *COL6A1* in their stromal cells, which matched our stroma cluster. Likewise, they reported high expression of *MYH11*, *MCAM*, *RGS5*, and *TAGLN* in smooth muscle cells, which corresponded to our pericytes. Their endothelial cells had high expression of *VWF* and *CDH5*, matching our endothelial cell cluster. These matches are also seen in fig. S6 (C and D and E and F). For immune cells, they identified a coarse group of cells expressing markers for T cells (*CD2*, *CD3G*, and *CD8A*) and antigen-presenting cells (*CD14* and *B2M*), while we identified four specific immune cell types. As explained above, we did not find granulosa cells in our scRNA-seq data. Rather, it was our spatial data that led to robust marker genes for each follicular cell type, which included canonical markers like *FOXL2*, *AMH*, and *INHBB* for granulosa; *CYP17A1*, *CYP11A1*, and *PTCH2* for theca; and dozens of previously unreported markers (Fig. 3C and data S5). By using our theca gene panels, we were able to suggest that a subset of Th/S cells in Fan *et al.* (*13*) could have been theca cells (fig. S6G), demonstrating how spatial data added value by complementing scRNA-seq data.

The RNA markers reported for the oocyte, theca cells, and granulosa cells in the ovary are among the strongest contributions of this study. While most of them await further in situ validation using RNA and protein immunostaining, we expect them to validate well, as the theca and granulosa ROI clusters are robust (Figs. 1, D and E and 3, A and B) and consistent across samples (Figs. 2D and3C). To aid the planning of such studies, we provided tiers of evidence based on literature references and previous knowledge of gene function (data S5). Some of these markers can be further developed into probes for isolating specific cell population for in-depth experimentation, such as being used to improve in vitro follicle culture or to promote the differentiation and maturation of stem cell–derived oocytes, instead of using fetal somatic cells (*37*, *38*), or they can be used in the isolation of steroidogenic cells expressing genes such as *STAR* and *CYP17A1* for hormone production in vitro. The markers may also be used for higher-resolution spatial analysis and lineage tracing, or as targets of perturbation to understand the wide range of disorders affecting the female reproductive system, such as female infertility, ovarian aging, or somatic aberrations that lead to cancers.

While the three marker panels seem robust, the findings for the cortex surface gradient (Fig. 4, A and B) and the gradient in the concentric rings around the oocyte (Fig. 3, D and E) are in need of replication in other samples and validation by in situ imaging. We acknowledge this as a major limitation of the current study. Meanwhile, our experience also underscored the limitations of the current ST technologies. For small functional units like the ovarian follicles, single-cell or even subcellular resolution is needed to fully elucidate the local cross-talk between the oocyte and its surrounding cell community. Highly multiplexed in situ imaging methods such as multiplexed error-robust fluorescence in situ hybridization (MERFISH) can measure the distribution of single RNA molecules for a few hundred RNA markers (*39*), and our lists of oocyte-, theca-, and granulosa-specific genes are essential and ideally suited for the optimal design of such gene panels. We expect that the rapidly improving resolution and multiplexity will soon allow us to study all stages of oocyte development, from the smallest primordial follicles to transitional and primary follicles and onward to antral follicles, the corpus luteum, and other events in follicle maturation and degeneration. The single-cell and spatial analyses we report here serve as a key step toward these more powerful data series, which are needed for understanding healthy ovarian function across the female reproductive life span, as well as disorders such as polycystic ovarian syndrome, premature ovarian aging, and ovarian cancers.

MATERIALS AND METHODS

Ethical approval process for cadaveric samples

This study used tissue samples from five deidentified deceased donors procured through the International Institute for the Advancement of Medicine (IIAM) and the associated Organ Procurement Organization (OPO) involved in collection. The use of cadaveric tissue in this research is categorized as "not regulated," per 45 CFR 46.102 and the "Common Rule," as it does not involve human subjects, and complies with the University of Michigan's Institutional Review Board requirements as such.

Ovarian donor tissue processing

All five donors were premenopausal, and examination of provided medical records indicated no pathological conditions affecting ovarian function (for their age, body mass index, recorded "race," and cold ischemic time; see fig. S1A). Before cross-clamp, the organs were perfused with Belzer University of Wisconsin Cold Storage Solution (Bridge of Life, SC, USA), Custodiol HTK (Histidine-Tryptophan-Ketoglutarate) Solution (Essential Pharmaceuticals, NC, USA), or SPS-1 Static Preservation Solution (Organ Recover Systems, IL, USA).

GeoMx ST experiments

Slide preparation and ROI sample collection

The cross sections of fresh ovarian tissue from donors 1 and 2 were resected from the central region of the organ along the short axis and then fixed in 4% paraformaldehyde (Fisher Scientific) for 24 hours at 4°C and rinsed five times for 24 hours each in Dulbecco's phosphate-buffered saline without calcium or magnesium ($DPBS^{-/-}$) at 4°C. The tissue was then embedded in paraffin for sectioning. Every other 5-μm section was stained with hematoxylin and eosin (H&E; Fisher Scientific) to select an unstained slide for spatial analysis. The selected

slides from donors 1 and 2 were deparaffinized and rehydrated, followed by antigen retrieval for 15 min at 90°C in tris-EDTA (Fisher Scientific). RNA targets were exposed using proteinase K (1 μg/ml) in PBS for 15 min at 37°C. For in situ hybridization, GeoMx reagents and protocols were used according to the manufacturer's instructions. The slide was stained with morphology markers before RNA collection. For donor 1, we used SYTO82 (a nuclei marker, Thermo Fisher Scientific, USA) and three protein markers: anti–smooth muscle actin to visualize pericytes and smooth muscle cells (SMA; α–smooth muscle actin monoclonal antibody conjugated to Alexa Fluor 488, Thermo Fisher Scientific, USA), anti-Ki67 to visualize proliferating cells (rabbit monoclonal 9027S, Cell Signaling Technology, USA), and anti-CD68 (sc-20060 AF594, Santa Cruz Biotechnology, USA). For donor 2, we again used SYTO82 and anti-CD68, along with anti-DAZL to visualize oocytes (MCA2336, Bio-Rad, USA) and anti-PGR to visualize cells expressing PGR such as luteinized follicular cells (ab63605, Abcam, USA).

NanoString library preparation and sequencing

The prepared slide was covered with Buffer S (NanoString, USA) and loaded into the NanoString GeoMx DSP instrument, which uses digital images of a slide-mounted tissue section, with up to four fluorescently labeled markers, to guide the selection of ROIs. ROIs are defined by the user based on cell morphology and related tissue features, using the "polygon," "contour," and "segmentation" tools provided in GeoMx DSP. Target enrichment ROIs were segmented into AOIs based on staining for CD68, Ki67, SMA, DAZL, and PGR. To collect concentric ROIs from ovarian follicles, a mask was designed in ImageJ (*40*) and imposed on the follicle's region in the tissue.

In this experiment, RNA molecules are affixed by photocleavable linkers; then, programmable ultraviolet light is used to release RNA from each ROI. RNA samples are collected by microcapillary aspiration into microtiter wells for sequencing-based analysis. In some cases, the selection was aided by histological images of one or both of the flanking tissue sections, which were not used for sample collection. Some of the ROIs are serial subdivisions of the same morphological area to capture local spatial changes. Some of the ROIs produced two to three AOIs/samples each due to targeted enrichment using one or two of the protein markers. Each sample is associated with additional information about its location, surface area (μm^2), and number of nuclei (an estimate of cell number) (data S1).

NanoString statistical analysis

We used the GeoMx analysis software to process the NanoString data, including steps for read decoding, trimming, and deduplication, and obtained the gene-by-sample read count data for 18,676 genes passing GeoMx's default quality control (QC) criteria. This is after removing gene #1309, "NegProbe-WTX," from the original data matrix. For donor 1, we initially collected 94 samples; however, two yielded fewer than 100,000 reads and were removed, leaving 92 samples, which came from 74 ROIs. They represent 14 "ROI types," as described in Fig. 1F and data S1. The 92 samples had library size (i.e., total read count) ranging from 146,463 to 4,464,464 (mean = 805,579), surface area ranging from 7619 to 359,037 μm^2 (mean = 60,591 μm^2), and nuclei counts ranging from 0 to 2544 (mean = 424) (data S1). Raw counts, which were already floored at 1 rather than 0 by NanoString, were normalized into counts per million (CPM), then log-transformed with base 2, and quantile-normalized. These 92-sample normalized data were used in the analyses shown in Fig. 3A. For all other analyses presented, we condensed the target-enriched AOIs from the same ROI into a single sample by summing up the reads over the AOIs, leading to the reduction of 29 AOIs to 11 ROIs, and the total sample number from 92 to 74. These 74 samples were similarly normalized to CPM, $\log_2$-transformed, quantile-normalized, and subjected to PCA and *k*-means clustering ($k = 6$) shown in Fig. 1D. We also observed that ROIs collected using an anti-Ki67 antibody (intended to target proliferating cells) showed poor antibody localization and low ROI expression of Ki67.

For donor 2, the 165 samples from 147 ROIs were normalized to CPM, $\log_2$-transformed, and quantile-normalized, with PCA and *k*-means clustering ($k = 9$) shown in Fig. 1E and figs. S1E, S2B, and S4B. The 165 samples from donor 2 had library sizes ranging from 24,862 to 3,404,417 (mean = 506,800), surface area ranging from 577 to 113,205 μm^2 (mean = 30,152 μm^2), and nuclei counts ranging from 0 to 1497 (mean = 240) (data S1). ROI selection for donor 2 covered 12 ROI types, including 7 of the 14 ROI types analyzed in donor 1 and 5 additional ROI types, bringing the total to 19.

While the analyses were based on NanoString's floor = 1 raw counts data, we examined an alternative method: minus 1 on all counts data, recalculate CPM, and then obtain $\log_2(\text{CPM} + 1)$. We found that the difference is minor in terms of the PCA projection of the 92 sample; thus, we opted to stay with the $\log_2$(CPM) method on the original, floor = 1 data. The quantile-normalized data for 74 ROI-based samples for donor 1 and the 165 AOI-based samples for donor 2 were shown in Figs. 2D and3C for the marker genes for oocyte, theca cells, and granulosa cells, as discussed in the main text. These quantile-normalized data were also used in PCA for subsets of samples, shown in Figs. 3B and4D and fig. S4 (B to D). For Figs. 2D and3C, the expression values for each gene were standardized for the 74 donor 1 samples and the 165 donor 2 samples separately, and shown in the heatmaps with a symmetrical, blue-to-red color palette. Here, "standardized" means centering by the mean and scaling by the SD.

Cluster analysis of NanoString data

For donor 1, PC1-PC2 in Fig. 1D revealed the separation of five clusters (C1 to C5). The sole oocyte sample separated itself in PC3 (fig. S1C) and was designated cluster 6 (C6). For donor 2, clustering was performed on all 165 samples (without consolidation of target-enriched samples) to highlight the unique signature of primordial/primary oocytes (ROI type #4) captured by DAZL, with *k*-means clustering ($k = 9$) shown in Fig. 1E. Centroid data, using the post-log transformation and quantile normalization data, for the six clusters from donor 1 and the nine clusters from donor 2, are included in data S2.

DE analysis

We performed 17 series of DE analysis for donor 1 using the quantile-normalized $\log_2$(CPM) data for 74 ROIs. Each DE analysis compares two groups of ROIs, as described below, and produced four statistics: fold change (FC), *t* score, raw *P* value, and adjusted *P* value, i.e., the Benjamini-Hochberg FDR (all provided in data S3). FC is reported on the $\log_2$ scale, and the *t* score is from *t* test without assuming equal variance in the two groups being compared.

The 17 DE series for donor 1 are for comparing samples in each cluster with those in all other clusters (cluster1vsAll, cluster2vsAll, cluster3vsAll, cluster4vsAll, and cluster5vsAll), comparing one cluster with its "adjacent" cluster (cluster1vs2, cluster2vs3, cluster3vs4, and cluster4vs5), and comparing target-enriched areas against their matched unenriched AOIs using paired *t* test: *SMA* (SMA^+ areas against their matched, untargeted area), *CD68* ($CD68^+$ areas against their matched, untargeted area), *Ki67* ($Ki67^+$ areas against their

matched, untargeted area), gradient in the cortex surface (linear regression across the 11 consecutive cortex surface layers, Fig. 4B), in *Ring34* (regression across the four consecutive cumulus cell rings around antral follicle 1, shown in Fig. 3, D and E), *Ring52* (regression across the five consecutive rings around the secondary follicle), cluster6vsAll (only FC, as there is only one sample in cluster 6), and cluster5vs6 (only FC). The five sets of one-cluster-versus-all-other comparison (such as cluster1vsAll) are based on the 73 ROIs without using the oocyte sample. Positive FC and *t* score values indicate that the expression is higher in this one cluster. In the four sets of one-cluster-versus-the-adjacent comparison (such as cluster1vs2), positive FC and *t* score values indicate that the expression is higher in the second higher numbered cluster. The three DE results for targeted AOIs are based on paired *t* tests for SMA (eight pairs), CD68 (three pairs), and Ki67 (seven pairs). Positive values mean higher expression in the enriched AOIs. This analysis relied on the 29 targeted samples from the 11 ROIs, using quantile normalization among the 29 rather than the quantile-normalized data across the entire set of 92 or 74 samples. In the cortex layer gradient analysis, positive values mean higher expression toward the surface. FC is the fitted slope over the series of layer numbers, 1 to 11. Since all FCs are in the $\log_2$ scale, a slope of 1/11 means an FC of 0.0909 per layer, or an FC of 1.0 overall, or twofold increase after 11 layers, spanning about 330 μm. In antral follicle 2, the oocyte is not present in the sampled section, although it is discernible in the H&E image of the adjacent section. For the regression result of the gradient across the four rings in "Ring34" and five rings in "Ring52," positive values mean higher expression toward the outside of the follicle. FC is the slope in the unit of per-ring. For instance, in ring34, an FC of one of four would mean an FC of one overall, or twofold change between the first and the fourth ring. Note that the center ROI of follicle, for both ring34 and ring52, was not used in the regression.

For donor 2, we performed 12 series of DE analysis using the quantile-normalized $\log_2$(CPM) data for all 165 ROIs. Each DE analysis compares two groups of ROIs, as described below, and produced the same four statistics: FC, *t* score, *P* value, and FDR-adjusted *P* value, which are all provided in data S3. The 12 DE series are as follows: cumulus versus non-cumulus granulosa (ROI type #13 versus type #12, denoted d13.12), theca versus granulosa (ROI type #14 versus types #12 and #13, denoted d14.1312), oocyte versus other (ROI type #4, $n = 11$, versus the other 154 ROIs, denoted oocyte.other), medulla versus similar cortex (cluster 5, $n = 38$, versus cluster 2, $n = 28$, denoted d5.2), granulosa versus other (ROI types #12 and #13, $n = 18$, versus all other ROIs minus the 11 samples for primordial and primary oocytes, $n = 136$, designed to be comparable to donor 1 granulosa DE results, denoted gc.other), theca versus other (ROI type #14, $n = 7$, versus all other ROIs minus primordial and primary oocytes, $n = 118$, designed to be comparable to donor 1 theca DE results, denoted tc.other), ovarian cyst versus other cortex (cluster 3, for ovarian cyst, $n = 21$ versus cluster 1, $n = 16$, denoted d3.1), within-cortex comparison (cluster 2 cortex samples, $n = 28$, versus clusters 1 and 3, $n = 37$, denoted d2.13), CD68-enriched ($n = 6$) versus all other ROIs minus primordial and primary oocytes ($n = 130$) (designed to be comparable to donor 1 CD68-enriched DE results, denoted cd68.other), medulla versus proximal cortex (cluster 5 medulla samples, $n = 38$, versus cluster 1 and 3 cortex samples, $n = 37$, denoted d5.13), medulla versus all cortex (cluster 5 medulla samples, $n = 38$, versus cluster 1 to 3 cortex samples, $n = 65$, denoted d5.123), and follicle rich versus follicle null (the nine $DAZL^+$ AOIs versus surface-most samples from the three cortex series, ROIs #61, #67, and #95, denoted richvnull, shown in Fig. 4E).

Pathway analysis of DE results

We used LRpath (*48*) to examine the enrichment pattern of Kyoto Encyclopedia of Genes and Genomes (KEGG) and Gene Ontology (GO) terms in each of the DE results. We converted gene symbols to Entrez IDs and uploaded the *P* value (for ranking significance) and FC (for direction of change) as input data. We selected "directional analysis" to separate enrichment signals for up- and down-regulation. For all 8423 GO and KEGG terms and each DE series, we collected odds ratio (OR) of enrichment, *P* value, and FDR. When OR > 1, the genes in this pathway are enriched among those with positive *t* scores in the gene-level analysis. For the two DE analyses involving donor 1 cluster 6, since there is only one oocyte sample and only FC (with *t* score or *P* value), we created a mock *P* value based on FC so that both significance rank and direction are available in the input file. All results are provided in data S4. For some of the comparisons, we only evaluated pathways with positive *t* scores (OR > 1), as the other direction is the "background" (e.g., one cluster versus all other). Note that pathway terms with too few genes tend to be noisy and have less significant *P* values. Those with too many genes tend to have significant *P* values even when the enrichment ratio is moderate.

Identification of marker genes for oocyte, theca cells, and granulosa cells

The 76 oocyte marker genes (Fig. 3D) came from the oocyte versus other FC > 2. The 45 theca cell marker genes (Fig. 4C) came from theca versus granulosa FC > 1.2 and theca versus other FC > 1, minus one gene that also appeared in the 76 oocyte markers. The 94 granulosa cell marker genes (Fig. 4C) came from theca versus granulosa FC < (−1) and granulosa versus other FC > 1.5, minus two genes that also appeared in the 76 oocyte markers.

scRNA-seq experiments using 10X Chromium

Tissue dissociation, cell sorting, and sequencing data collection

We collected scRNA-seq data from three additional donors (fig. S1A). Upon arrival, ovarian tissue (cortex and medulla) from donors 3 to 5 was chopped into ~1-mm cubes at room temperature in Quinn's Advantage Medium with Hepes (CooperSurgical, Denmark) with 10% Quinn's Advantage Serum Protein Substitute (CooperSurgical). These tissue cubes were rinsed twice with $DPBS^{-/-}$ (Fisher Scientific, USA) and then transferred to a digestion solution containing collagenase IA (0.5 mg/ml; Sigma-Aldrich, Germany) and deoxyribonuclease I (0.01 mg/ml; Worthington Biochemical, USA) in DPBS with calcium and magnesium ($DPBS^{+/+}$, Fisher Scientific). Tissue was transferred to a shaker of 150 rpm to digest for 30 min at 37°C, and then the tissue was strained through a 70-μm strainer (Fisher Scientific), followed by a 30-μm strainer (PluriSelect, USA). The cell suspension was quenched with ice-cold 10% fetal bovine serum (Fisher Scientific) in $DPBS^{-/-}$. The remaining tissue with undissociated cells was placed in fresh digestion solution and shaken for an additional 30 min before straining and quenching. Cell suspensions were stored on ice and treated with red blood cell lysis buffer (BioLegend, USA) according to the manufacturer's instructions. Suspensions were then rinsed in 1% bovine serum albumin (BSA; Fisher Scientific) in $DPBS^{-/-}$ followed by 0.04% BSA in $DPBS^{-/-}$ to remove debris. Cells were pelleted at 100*g* for 5 min between all rinsing steps. Cortex and medulla were enzymatically digested separately and then combined into a single-cell suspension at a 1:1 ratio.

Combined cortex/medulla single-cell suspensions from tissue dissociation were incubated with 3 μM 4′,6-diamidino-2-phenylindole, dihydrochloride (DAPI; Fisher Scientific) per 1 million cells for 30 min on ice in preparation for fluorescence-activated cell sorting (FACS) at the University of Michigan's Flow Cytometry Core. Cells were sorted on a MoFlow Astrios (Beckman Coulter, USA) to remove dead cells ($DAPI^+$) and collect live cells ($DAPI^-$). FlowJo v10 software was used for gating and cell counting. We performed three runs of scRNA-seq using dissociated cells from donors 3, 4, and 5, respectively, thus creating three experimental batches. Freshly sorted cells were submitted to the Advanced Genomics Core at the University of Michigan, loaded to the 10X Genomics Chromium controller for droplet-based single-cell capture. Cell lysis and RNA-seq library preparation used the Chromium Next GEM Single Cell 3′ LT Kit according to the manufacturer's instructions. Libraries were sequenced on NovaSeq F0 using an S4 flow cell. The Core performed basic QC and read alignment using standard procedures, and provided unique molecular identifier (UMI) counts data in a cell-by-gene matrix for each sample.

Statistical analysis

ScRNA data from the three donors were initially processed by the Univerisity of Michigan Advanced Genomics Core using Cell Ranger v4.0.0. The main steps include the extraction of cell barcodes and the UMIs from the raw paired-end sequencing reads, alignment to human Ensembl genes, and UMI-based deduplication, leading to a cell-by-gene UMI count table, represented by the "filtered_feature_bc_matrix" for 14,322, 13,901, and 9149 cells for the three samples, respectively, for 20,886 genes.

Downstream analysis used a combination of Seurat and custom codes in R. Cell filtering used (i) minimal number of UMI (called "nCount" in Seurat) and (ii) % of transcripts corresponding to mitochondria-encoded genes ("% MT"). The cutoff values varied for the three samples: nCount: 2300, 1275, and 1096; % MT: 15, 12, and 15, respectively. The cutoffs were chosen on the basis of each sample's distribution of nCount and % MT (not shown). After filtering, there are 7571, 7228, and 6339 cells left for further analysis. The average of nCount, number of genes detected ("nFeature"), and % MT for these cells are shown in fig. S1A.

Identification of major cell types

We normalized the counts data to CPM and analyzed the $\log_2(\text{CPM}+1)$ data for the three donors separately. Initial analyses showed that donor 5 contained the greatest proportion of nonstromal cells, and we analyzed this donor's 6339 cells first. We selected 2034 genes of high expression and high variability for PCA and used the top 50 PCs for *k*-means cluster ($k = 14$) and *t*-SNE projection (Fig. 5A). The 14 clusters can be merged to five main clusters (Fig. 5A), corresponding to stroma cells, two apparent subtypes of immune cells, pericyte, and endothelial cells, as annotated by marker gene expression (Fig. 5, C and D). Of the 6339 cells, 5399 (85.2%) were stromal cells.

For donors 3 and 4, since the stromal cells dominated more strongly than in donor 5, *k*-means clustering could not readily separate the nonstromal cells, although they appeared in distinct clusters in *t*-SNE (fig. S5, A and B). We used the centroids of the five main cell types in donor 5 to perform supervised annotation for cells in donors 3 and 4 (i.e., a cell is assigned to a cell type by the maximal correlation among the five centroids), with the resulting cell label shown in fig. S5 (A and B). For donors 3 and 4, the analyses proceeded by the selection of 3702 and 2251 genes, respectively, that were highly expressed and highly variable, followed by PCA and *t*-SNE projection using the top 50 PCs. After supervised cell annotation, 7438 of the 7571 cells (98.2%) in donor 3, and 7052 of the 7228 cells (97.6%) in donor 4, were stromal cells. Marker genes shown in Fig. 5D came from a series of DE analyses comparing one cell type against the other, as was done for the immune cell types described below.

Identification of four immune cell types

For immune cells, we combined the 59, 133, and 671 immune cells from donors 3, 4, and 5, respectively, and reran PCA for these 863 cells. Uniform Manifold Approximation and Projection (UMAP) projection using the top 20 PCs revealed four immune cell subtypes (Fig. 5B). Marker-based annotation (Fig. 5, C and D) identified them as NK cells ($n = 105$), T cells ($n = 409$), macrophage ($n = 319$), and mast cells ($n = 30$).

Lack of heterogeneity among stromal cells

We attempted to identify subtypes of stromal cells or gradients among them that could reflect shifting regulatory states. We observed that the stromal cells in our datasets were notably uniform in their expression profile. The donor-to-donor variation (i.e., the "batch effect"), while not a prominent factor in the identification of major cell types or immune cell subtypes (as shown in Fig. 5), became dominant when characterizing the variation among stromal cells. Further, slight changes in gene selection, or in the algorithm dealing with the 0-counts (e.g., using CPM or CPK—counts per thousand), markedly altered PCA, subsequent UMAP or *t*-SNE projection, or the *k*-means clustering results. Most projections and clustering solutions were driven by the cells' "library size," hence by their length of 0- and 1-counts, suggesting that there is no discernible heterogeneity among the stromal cells.

For instance, among the 5399 stromal cells in donor 5, we selected 4881 cells of the largest library size and then selected 3473 most highly expressed genes for use in PCA and in *t*-SNE projection using the top 50 PCs. In parallel, we reran quantile normalization using the 4881-by-3473 data and subsequent PCA and *t*-SNE. In the third option, we "imputed" 0 CPM values in each sample with the half of the minimal nonzero CPM value, calculated CPM again, and ran quantile normalization of $\log_2$(new-CPM), followed by PCA and UMAP and *t*-SNE projections. In additional tries, we ran analysis on a more stringent set of 2122 cells and repeated the procedure on donor 3 and 4 stromal cells with multiple selections of the strongest cells and strongest genes. In all case, the projections failed to reveal separate groups of cells (not shown), and the persistent unimodal distribution was driven by gradients of library size.

In an alternative, supervised approach, we took advantage of the robust gene sets from the NanoString data for oocytes, theca cells, and granulosa cells (Figs. 2D and3C) to calculate an oocyte score, a theca score, and a granulosa score for each stromal cell. This is essentially an attempt to identify the rare subsets of stromal cells that could have been oocytes or theca or granulosa cells that were difficult to uncover using unsupervised approaches. For each cell, we summed the expression values over the 76 oocyte marker genes, 45 theca markers, and 94 granulosa markers, in either the linear CPM space or the log(CPM + 1) space (or CPM imputed with half-minimal values), with or without normalizing each cell's score by its library size, in either the linear or the log space. Of all the combinatorial options of constructing such scores, a few showed that some cells seemed to have a theca-like character and were near each other in UMAP, and some of them also showed a granulosa-like character. An example is shown in fig. S5B. However, they do not appear as a distinct subtype of stromal cells. There is no evidence that cells at the periphery of the UMAP projection

were hybrid cells with nonstromal cells (using markers for major cell types; not shown).

Comparisons with previous single-cell studies

We downloaded the scRNA-seq data from Fan *et al.* (*13*) and used Seurat to generate cell type centroids and *t*-SNE projection shown in fig. S6G. The centroid-centroid correlations in fig. S6A were calculated using 442 genes, which is the overlap between 2000 highly variable genes (HVGs) in our data and the 2000 HVGs in Fan *et al.* (*13*). The centroid-centroid correlations with Wagner *et al.* (*9*) data (fig. S6C) used 469 genes that overlapped between 2000 HVGs in our data and 2000 HVGs in the Wagner study. Marker gene expression in fig. S6 (B and D) used gene lists from data S5 and ordered in the same way, with each gene's values centered by mean and scaled by SD across the centroids in the Fan data and the Wagner data. The correlations shown in fig. S6E are Spearman's correlation coefficients using all 15,510 genes that overlapped between the Fan study and our study, while those in fig. S6F are Spearman's correlation coefficients using 1907 genes, which is the overlap of our 2000 HVGs and all genes in the Wagner study. Cluster labels in fig. S6G (left) were downloaded from Fan *et al.* (*13*). The theca score for the cells in the Fan study (fig. S6G, right) is calculated as the sum of log(CPM + 1) values over the 45 theca marker genes. Correlations in fig. S6H used our 2000 HVGs within the immune cells, reduced to 426 genes by overlapping with Fan's 2000 HVGs.

Supplementary Materials

This PDF file includes:

Figs. S1 to S6
Legends for data S1 to S8
References

Other Supplementary Material for this manuscript includes the following:

Data S1 to S8

REFERENCES AND NOTES

1. K. Hummitzsch, H. F. Irving-Rodgers, J. Schwartz, R. J. Rodgers, Development of the mammalian ovary and follicles, in *The Ovary* (Elsevier, 2019), pp. 71–82.
2. K. E. O'Neill, J. Y. Maher, M. M. Laronda, F. E. Duncan, R. D. LeDuc, M. E. Lujan, K. H. Oktay, A. M. Pouch, J. H. Segars, E. L. Tsui, M. B. Zelinski, L. M. Halvorson, V. Gomez-Lobo, Anatomic nomenclature and 3-dimensional regional model of the human ovary: Call for a new paradigm. *Am. J. Obstet. Gynecol.* **228**, 270–275.e4 (2023).
3. D. L. Russell, R. L. Robker, Ovulation: The coordination of intrafollicular networks to ensure oocyte release, in *The Ovary* (Elsevier, 2019), pp. 217–234.
4. H. M. Kinnear, C. E. Tomaszewski, F. L. Chang, M. B. Moravek, M. Xu, V. Padmanabhan, A. Shikanov, The ovarian stroma as a new frontier. *Reproduction* **160**, R25–R39 (2020).
5. A. S. K. Jones, A. Shikanov, Follicle development as an orchestrated signaling network in a 3D organoid. *J. Biol. Eng.* **13**, 2 (2019).
6. J. K. Findlay, K. R. Dunning, R. B. Gilchrist, K. J. Hutt, D. L. Russell, K. A. Walters, Follicle selection in mammalian ovaries, in *The Ovary* (Elsevier, 2019), pp. 3–21.
7. E. Nilsson, M. K. Skinner, Cellular interactions that control primordial follicle development and folliculogenesis. *J. Soc. Gynecol. Invest.* **8**, S17–S20 (2001).
8. M. E. Morris, M. C. Meinsohn, M. Chauvin, H. D. Saatcioglu, A. Kashiwagi, N. A. Sicher, N. Nguyen, S. Yuan, R. Stavely, M. Hyun, P. K. Donahoe, B. L. Sabatini, D. Pépin, A single-cell atlas of the cycling murine ovary. *eLife* **11**, e77239 (2022).
9. M. Wagner, M. Yoshihara, I. Douagi, A. Damdimopoulos, S. Panula, S. Petropoulos, H. Lu, K. Pettersson, K. Palm, S. Katayama, O. Hovatta, J. Kere, F. Lanner, P. Damdimopoulou, Single-cell analysis of human ovarian cortex identifies distinct cell populations but no oogonial stem cells. *Nat. Commun.* **11**, 1147 (2020).
10. E. Ouni, D. Vertommen, M. C. Chiti, M.-M. Dolmans, C. A. Amorim, A draft map of the human ovarian proteome for tissue engineering and clinical applications. *Mol. Cell. Proteomics* **18**, S159–S173 (2019).
11. O. Hovatta, C. Wright, T. Krausz, K. Hardy, R. M. L. Winston, Human primordial, primary and secondary ovarian follicles in long-term culture: Effect of partial isolation. *Hum. Reprod.* **14**, 2519–2524 (1999).
12. E. E. Telfer, M. McLaughlin, C. Ding, K. J. Thong, A two-step serum-free culture system supports development of human oocytes from primordial follicles in the presence of activin. *Hum. Reprod.* **23**, 1151–1158 (2008).
13. X. Fan, M. Bialecka, I. Moustakas, E. Lam, V. Torrens-Juaneda, N. V. Borggreven, L. Trouw, L. A. Louwe, G. S. K. Pilgram, H. Mei, L. van der Westerlaken, Single-cell reconstruction of follicular remodeling in the human adult ovary. *Nat. Commun.* **10**, 3164 (2019).
14. P. Yurttas, A. M. Vitale, R. J. Fitzhenry, L. Cohen-Gould, W. Wu, J. A. Gossen, S. A. Coonrod, Role for PADI6 and the cytoplasmic lattices in ribosomal storage in oocytes and translational control in the early mouse embryo. *Development* **135**, 2627–2636 (2008).
15. I. M. A. Jentoft, F. J. B. Bäuerlein, L. M. Welp, B. H. Cooper, A. Petrovic, C. So, S. M. Penir, A. Z. Politi, Y. Horokhovskyi, I. Takala, H. Eckel, R. Moltrecht, P. Lénárt, T. Cavazza, J. Liepe, N. Brose, H. Urlaub, R. Fernández-Busnadiego, M. Schuh, Mammalian oocytes store proteins for the early embryo on cytoplasmic lattices. *Cell* **186**, 5308–5327.e25 (2023).
16. G. Esposito, A. M. Vitale, F. P. J. Leijten, A. M. Strik, A. M. C. B. Koonen-Reemst, P. Yurttas, T. J. A. A. Robben, S. Coonrod, J. A. Gossen, Peptidylarginine deiminase (PAD) 6 is essential for oocyte cytoskeletal sheet formation and female fertility. *Mol. Cell. Endocrinol.* **273**, 25–31 (2007).
17. N. R. Mtango, M. Sutovsky, A. Susor, Z. Zhong, K. E. Latham, P. Sutovsky, Essential role of maternal UCHL1 and UCHL3 in fertilization and preimplantation embryo development. *J. Cell. Physiol.* **227**, 1592–1603 (2012).
18. R. Kumar, C. Oliver, C. Brun, A. B. Juarez-Martinez, Y. Tarabay, J. Kadlec, B. De Massy, Mouse REC114 is essential for meiotic DNA double-strand break formation and forms a complex with MEI4. *Life Sci. Alliance* **1**, e201800259 (2018).
19. S. Llonch, M. Barragán, P. Nieto, A. Mallol, M. Elosua-Bayes, P. Lorden, S. Ruiz, F. Zambelli, H. Heyn, R. Vassena, B. Payer, Single human oocyte transcriptome analysis reveals distinct maturation stage-dependent pathways impacted by age. *Aging Cell* **20**, 1–18 (2021).
20. A. Abedini, G. Zamberlam, E. Lapointe, C. Tourigny, A. Boyer, M. Paquet, K. Hayashi, H. Honda, A. Kikuchi, C. Price, D. Boerboom, WNT5a is required for normal ovarian follicle development and antagonizes gonadotropin responsiveness in granulosa cells by suppressing canonical WNT signaling. *FASEB J.* **30**, 1534–1547 (2016).
21. P. J. Ansell, Y. Zhou, B.-M. Schjeide, A. Kerner, J. Zhao, X. Zhang, A. Klibanski, Regulation of growth hormone expression by delta-like protein 1 (Dlk1). *Mol Cell Endocrinol.* **271**, 55–63 (2007).
22. P. Puri, L. Little-Ihrig, U. Chandran, N. C. Law, M. Hunzicker-Dunn, A. J. Zeleznik, Protein kinase A: A master kinase of granulosa cell differentiation. *Sci. Rep.* **6**, 1 (2016).
23. E. Ouni, C. Bouzin, M. M. Dolmans, E. Marbaix, Spatiotemporal changes in mechanical matrisome components of the human ovary from prepuberty to menopause. *Hum. Reprod.* **35**, 1391–1410 (2020).
24. B. Bagalad, K. M. Kumar, H. Puneeth, Myofibroblasts: Master of disguise. *J. Oral Maxillofac. Pathol.*, *21*, 462–463 (2017).
25. S. C. Hewitt, K. S. Korach, Estrogen receptors: New directions in the new millennium. *Endocr. Rev.* **39**, 664–675 (2018).
26. H. Zhou, Y. Pon, A. Wong, HGF/MET signaling in ovarian cancer. *Curr. Mol. Med.* **8**, 469–480 (2008).
27. F. Chen, Y. Wu, L. Ke, X. Lin, F. Wang, Y. Qin, ARHGEF15 in Sertoli cells contributes to germ cell development and testicular immune privilege. *Biol. Reprod.* **107**, 1565–1579 (2022).
28. Q. Zhuge, Z. Wu, L. Huang, B. Zhao, M. Zhong, W. Zheng, C. Gourong, X. Mao, L. Xie, X. Wang, K. Jin, Notch4 is activated in endothelial and smooth muscle cells in human brain arteriovenous malformations. *J. Cell. Mol. Med.* **17**, 1458–1464 (2013).
29. H. Pinkas, B. Fisch, G. Rozansky, C. Felz, G. Kessler-Icekson, H. Krissi, S. Nitke, A. Ao, R. Abir, Platelet-derived growth factors (PDGF-A and -B) and their receptors in human fetal and adult ovaries. *Mol. Hum. Reprod.* **14**, 199–206 (2008).
30. A. Naba, K. R. Clauser, S. Hoersch, H. Liu, S. A. Carr, R. O. Hynes, The matrisome: In silico definition and in vivo characterization by proteomics of normal and tumor extracellular matrices. *Mol. Cell. Proteomics* **11**, M111.014647 (2012).
31. Y. Ni, C. Ji, B. Wang, J. Qiu, J. Wang, X. Guo, A novel pro-adipogenesis factor abundant in adipose tissues and over-expressed in obesity acts upstream of PPARγ and C/EBPα. *J. Bioenerg. Biomembr.* **45**, 219–228 (2013).
32. L. L. Espey, T. Ujioka, D. L. Russell, M. Skelsey, B. Vladu, R. L. Robker, H. Okamura, J. S. Richards, Induction of early growth response protein-1 gene expression in the rat ovary in response to an ovulatory dose of human chorionic gonadotropin. *Endocrinology* **141**, 2385–2391 (2000).
33. P. Asiabi, M. M. Dolmans, J. Ambroise, A. Camboni, C. A. Amorim, In vitro differentiation of theca cells from ovarian cells isolated from postmenopausal women. *Hum. Reprod.* **35**, 2793–2807 (2020).
34. J. A. S. Richards, Y. A. Ren, N. Candelaria, J. E. Adams, A. Rajkovic, Ovarian follicular theca cell recruitment, differentiation, and impact on fertility: 2017 update. *Endocr. Rev.* **39**, 1–20 (2018).
35. N. L. Guahmich, L. Man, J. Wang, L. Arazi, E. Kallinos, A. Topper-Kroog, G. Grullon, K. Zhang, J. Stewart, N. Schatz-Siemers, S. H. Jones, R. Bodine, N. Zaninovic, G. Schattman,

Z. Rosenwaks, D. James, Human theca arises from ovarian stroma and is comprised of three discrete subtypes. *Commun. Biol.* **6**, 1–15 (2023).
36. K. Ridinger, S100A13: Biochemical characterization and subcellular localization in different cell lines. *J. Biol. Chem.* **275**, 8686–8694 (2000).
37. R. A. Harris, J. M. McAllister, J. F. Strauss, Single-cell RNA-seq identifies pathways and genes contributing to the hyperandrogenemia associated with polycystic ovary syndrome. *Int. J. Mol. Sci.* **24**, 10611 (2023).
38. T. Yazawa, Y. Imamichi, T. Sekiguchi, K. Miyamoto, J. Uwada, M. R. I. Khan, N. Suzuki, A. Umezawa, T. Taniguchi, Transcriptional regulation of ovarian steroidogenic genes: Recent findings obtained from stem cell-derived steroidogenic cells. *Biomed. Res. Int.* **2019**, (2019).
39. T. Liu, Q. Y. Qin, J. X. Qu, H. Y. Wang, J. Yan, Where are the theca cells from: The mechanism of theca cells derivation and differentiation. *Chin. Med. J. (Engl).* **133**, 1711–1718 (2020).
40. J. Jin, P. Ren, X. Li, Y. Zhang, W. Yang, Y. Ma, M. Lai, C. Yu, S. Zhang, Y. L. Zhang, Ovulatory signal-triggered chromatin remodeling in ovarian granulosa cells by HDAC2 phosphorylation activation-mediated histone deacetylation. *Epigenetics Chromatin* **16**, 11 (2023).
41. E. Madogwe, D. K. Tanwar, M. Taibi, Y. Schuermann, A. St-Yves, R. Duggavathi, Global analysis of FSH-regulated gene expression and histone modification in mouse granulosa cells. *Mol. Reprod. Dev.* **87**, 1082–1096 (2020).
42. T. Kawai, J. A. S. Richards, M. Shimada, Large-scale DNA demethylation occurs in proliferating ovarian granulosa cells during mouse follicular development. *Commun. Biol.* **4**, 1334 (2021).
43. D. A. Demanno, J. E. Cottom, M. P. Kline, C. A. Peters, E. T. Maizels, M. Hunzicker-Dunn, Follicle-stimulating hormone promotes histone H3 phosphorylation on serine-10. *Mol. Endocrinol.* **13**, 91–105 (1999).
44. J. Jankovičová, P. Sečová, K. Michalková, J. Antalíková, Tetraspanins, more than markers of extracellular vesicles in reproduction. *Int. J. Mol. Sci.* **21**, 7568 (2020).
45. H. C. Alberico, D. C. Woods, Role of granulosa cells in the aging ovarian landscape: A focus on mitochondrial and metabolic function. *Front. Physiol.* **12**, 800739 (2021).
46. T. B. Papler, E. V. Bokal, A. Maver, A. N. Kopitar, L. Lovrečić, Transcriptomic analysis and meta-analysis of human granulosa and cumulus cells. *PLOS ONE* **10**, e0136473 (2015).
47. N. Hatzirodos, K. Hummitzsch, H. F. Irving-Rodgers, M. L. Harland, S. E. Morris, R. J. Rodgers, Transcriptome profiling of granulosa cells from bovine ovarian follicles during atresia. *BMC Genomics* **15**, 24 (2014).
48. J. H. Kim, A. Karnovsky, V. Mahavisno, T. Weymouth, M. Pande, D. C. Dolinoy, L. S. Rozek, M. A. Sartor, LRpath analysis reveals common pathways dysregulated via DNA methylation across cancer types. *BMC Genomics* **13**, 1 (2012).
49. Y. Ichikawa, M. Matsuzaki, S. Mizushima, T. Sasanami, Possible involvement of annexin A6 in preferential sperm penetration in the germinal disk region. *Reprod. Fertil.* **3**, 152–161 (2022).
50. A. Girard, I. Dufort, G. Douville, M. A. Sirard, Global gene expression in granulosa cells of growing, plateau and atretic dominant follicles in cattle. *Reprod. Biol. Endocrinol.* **13**, 17 (2015).
51. Y. Han, G. Xia, B. K. Tsang, Regulation of cyclin d2 expression and degradation by follicle-stimulating hormone during rat granulosa cell proliferation in vitro. *Biol. Reprod.* **88**, 57 (2013).
52. E. Chronowska, High-throughput analysis of ovarian granulosa cell transcriptome. *Biomed. Res. Int.* **2014**, 1–7 (2014).
53. F. Li, H. Jang, M. Puttabyatappa, M. Jo, T. E. Curry, Ovarian FAM110C (family with sequence similarity 110C): Induction during the periovulatory period and regulation of granulosa cell cycle kinetics in rats. *Biol. Reprod.* **86**, 185 (2012).
54. N. Hatzirodos, K. Hummitzsch, H. F. Irving-Rodgers, R. J. Rodgers, Transcriptome comparisons identify new cell markers for theca interna and granulosa cells from small and large antral ovarian follicles. *PLOS ONE* **10**, e0119800 (2015).
55. N. Qin, T. L. Tyasi, X. Sun, X. Chen, H. Zhu, J. Zhao, R. Xu, Determination of the roles of GREM1 gene in granulosa cell proliferation and steroidogenesis of hen ovarian prehierarchical follicles. *Theriogenology* **151**, 28–40 (2020).
56. Y. Yamaguma, N. Sugita, N. Choijookhuu, K. Yano, D. Lee, M. Ikenoue, Fidya, S. Shirouzu, T. Ishizuka, M. Tanaka, Y. Yamashita, E. Chosa, N. Taniguchi, Y. Hishikawa, Crucial role of high-mobility group box 2 in mouse ovarian follicular development through estrogen receptor beta. *Histochem. Cell Biol.* **157**, 359–369 (2022).
57. L. K. Christenson, S. Gunewardena, X. Hong, M. Spitschak, A. Baufeld, J. Vanselow, Research resource: Preovulatory LH surge effects on follicular theca and granulosa transcriptomes. *Mol. Endocrinol.* **27**, 1153–1171 (2013).
58. Y. Ma, J. Jin, X. Tong, W. Yang, P. Ren, Y. Dai, Y. Pan, Y. L. Zhang, S. Zhang, ADAMTS1 and HSPG2 mRNA levels in cumulus cells are related to human oocyte quality and controlled ovarian hyperstimulation outcomes. *J. Assist. Reprod. Genet.* **37**, 657–667 (2020).
59. K. H. Burns, G. E. Owens, J. M. Fernandez, J. H. Nilson, M. M. Matzuk, Characterization of integrin expression in the mouse ovary. *Biol. Reprod.* **67**, 743–751 (2002).
60. A. D. Stapp, B. I. Gómez, C. A. Gifford, D. M. Hallford, J. A. Hernandez Gifford, Canonical WNT signaling inhibits follicle stimulating hormone mediated steroidogenesis in primary cultures of rat granulosa cells. *PLOS ONE* **9**, 86432 (2014).
61. S. Granados-Aparici, A. Volodarsky-Perel, Q. Yang, S. Anam, T. Tulandi, W. Buckett, W. Y. Son, G. Younes, J. T. Chung, S. Jin, M. E. Terret, H. J. Clarke, MYO10 promotes transzonal projection-dependent germ line-somatic contact during mammalian folliculogenesis. *Biol. Reprod.* **107**, 474–487 (2022).
62. R. Kawagishi, M. Tahara, K. Morishige, M. Sakata, K. Tasaka, W. Ikeda, K. Morimoto, Y. Takai, Y. Murata, Expression of nectin-2 in mouse granulosa cells. *Eur. J. Obstet. Gynecol. Reprod. Biol.* **121**, 71–76 (2005).
63. H. Yoon, H. Jang, E. Y. Kim, S. Moon, S. Lee, M. Cho, H. J. Cho, J. J. Ko, E. M. Chang, K. A. Lee, Y. Choi, Knockdown of PRKAR2B results in the failure of oocyte maturation. *Cell. Physiol. Biochem.* **45**, 2009–2020 (2018).
64. J. P. Dong, Z. H. Dai, Z. X. Jiang, Y. He, L. Wang, Q. Y. Liao, N. X. Sun, Y. N. Wang, S. H. Sun, W. Lin, W. Li, F. Yang, CD24: A marker of granulosa cell subpopulation and a mediator of ovulation. *Cell Death Dis.* **10**, 791 (2019).
65. A. Baufeld, J. Vanselow, Lactate-induced effects on bovine granulosa cells are mediated via PKA signaling. *Cell Tissue Res.* **388**, 471–477 (2022).
66. Dou, Y. De, STMN1 promotes progesterone production via StAR up-regulation in mouse granulosa cells. *Sci. Rep.* **6**, 1–10 (2016).
67. X. Sun, X. Chen, J. Zhao, C. Ma, C. Yan, S. Liswaniso, R. Xu, N. Qin, Transcriptome comparative analysis of ovarian follicles reveals the key genes and signaling pathways implicated in hen egg production. *BMC Genomics* **22**, 899 (2021).
68. D. L. Russell, S. A. Ochsner, M. Hsieh, S. Mulders, J. S. Richards, Hormone-regulated expression and localization of versican in the rodent ovary. *Endocrinology* **144**, 1020–1031 (2003).
69. S. G. Kim, S. J. Jang, J. Soh, K. Lee, J. K. Park, W. K. Chang, E. W. Park, S. Y. Chun, Expression of ectodermal neural cortex 1 and its association with actin during the ovulatory process in the rat. *Endocrinology* **150**, 3800–3806 (2009).
70. I. Kugathas, H. K. L. Johansson, E. Chan Sock Peng, M. Toupin, B. Evrard, T. A. Darde, J. Boberg, M. K. Draskau, A. D. Rolland, S. Mazaud-Guittot, F. Chalmel, T. Svingen, Transcriptional profiling of the developing rat ovary following intrauterine exposure to the endocrine disruptors diethylstilbestrol and ketoconazole. *Arch. Toxicol.* **97**, 849–863 (2023).
71. S. C. Baumgarten, S. M. Convissar, A. M. Zamah, M. A. Fierro, N. J. Winston, B. Scoccia, C. Stocco, FSH regulates IGF-2 expression in human granulosa cells in an AKT-dependent manner. *J. Clin. Endocrinol. Metab.* **100**, E1046–E1055 (2015).
72. J. Lim, U. Luderer, Oxidative damage increases and antioxidant gene expression decreases with aging in the mouse ovary. *Biol. Reprod.* **84**, 775–782 (2011).
73. L. M. Jiménez, M. Binelli, K. Bertolin, R. M. Pelletier, B. D. Murphy, Scavenger receptor-B1 and luteal function in mice. *J. Lipid Res.* **51**, 2362–2371 (2010).
74. S. Itami, S. Tamotsu, A. Sakai, K. Yasuda, The roles of THY1 and integrin beta3 in cell adhesion during theca cell layer formation and the effect of follicle-stimulating hormone on THY1 and integrin beta3 localization in mouse ovarian follicles. *Biol. Reprod.* **84**, 986–995 (2011).
75. C. Joseph, M. G. Hunter, K. D. Sinclair, R. S. Robinson, The expression, regulation and function of secreted protein, acidic, cysteine-rich in the follicle-luteal transition. *Reproduction* **144**, 361–372 (2012).
76. M. Lim, H. M. Brown, R. D. Rose, J. G. Thompson, K. R. Dunning, Dysregulation of bisphosphoglycerate mutase during in vitro maturation of oocytes. *J. Assist. Reprod. Genet.* **38**, 1363–1372 (2021).
77. W. Fujii, T. Nishimura, K. Kano, K. Sugiura, K. Naito, CDK7 and CCNH are components of CDK-activating kinase and are required for meiotic progression of pig oocytes. *Biol. Reprod.* **85**, 1124–1132 (2011).
78. Y. Li, Z. Zhang, J. Chen, W. Liu, W. Lai, B. Liu, X. Li, L. Liu, S. Xu, Q. Dong, M. Wang, X. Duan, J. Tan, Y. Zheng, P. Zhang, G. Fan, J. Wong, G. L. Xu, Z. Wang, H. Wang, S. Gao, B. Zhu, Stella safeguards the oocyte methylome by preventing de novo methylation mediated by DNMT1. *Nature* **564**, 136–140 (2018).
79. M. Zhao, F. Feng, C. Chu, W. Yue, L. Li, A novel EIF4ENIF1 mutation associated with a diminished ovarian reserve and premature ovarian insufficiency identified by whole-exome sequencing. *J. Ovarian Res.* **12**, 119 (2019).
80. L. Yu, Loss of ESRP1 blocks mouse oocyte development and leads to female infertility. *Development* **148**, 1 (2021).
81. S. Markholt, M. L. Grøndahl, E. H. Ernst, C. Y. Andersen, E. Ernst, K. Lykke-Hartmann, Global gene analysis of oocytes from early stages in human folliculogenesis shows high expression of novel genes in reproduction. *Mol. Hum. Reprod.* **18**, 96–110 (2012).
82. Y. Tanaka, S. Kato, M. Tanaka, N. Kuji, Y. Yoshimura, Structure and expression of the human oocyte-specific histone H1 gene elucidated by direct RT-nested PCR of a single oocyte. *Biochem. Biophys. Res. Commun.* **304**, 351–357 (2003).
83. A. Metchat, M. Åkerfelt, C. Bierkamp, V. Delsinne, L. Sistonen, H. Alexandre, E. S. Christians, Mammalian heat shock factor 1 is essential for oocyte meiosis and directly regulates Hsp90α expression. *J. Biol. Chem.* **284**, 9521–9528 (2009).
84. X. Wang, K. E. Park, S. Koser, S. Liu, L. Magnani, R. A. Cabot, KPNA7, an oocyte- and embryo-specific karyopherin α subtype, is required for porcine embryo development. *Reprod. Fertil. Dev.* **24**, 382–391 (2012).

85. P. Zhang, M. Dixon, M. Zucchelli, F. Hambiliki, L. Levkov, O. Hovatta, J. Kere, Expression analysis of the NLRP gene family suggests a role in human preimplantation development. *PLOS ONE* **3**, e2755 (2008).
86. X. Wang, W. Rosikiewicz, Y. Sedkov, T. Martinez, B. S. Hansen, P. Schreiner, J. Christensen, B. Xu, S. M. Pruett-Miller, K. Helin, H. M. Herz, PROSER1 mediates TET2 O-GlcNAcylation to regulate DNA demethylation on UTX-dependent enhancers and CpG islands. *Life Sci. Alliance* **5**, e202101228 (2022).
87. M. H. Sun, L. L. Hu, C. Y. Zhao, X. Lu, Y. P. Ren, J. L. Wang, X. S. Cui, S. C. Sun, Ral GTPase is essential for actin dynamics and Golgi apparatus distribution in mouse oocyte maturation. *Cell Div.* **16**, 1–12 (2021).
88. M. L. Bernhardt, K. M. Lowther, E. Padilla-Banks, C. E. McDonough, K. N. Lee, A. V. Evsikov, T. F. Uliasz, P. Chidiac, C. J. Williams, L. M. Mehlmann, Regulator of G-protein signaling 2 (RGS2) suppresses premature calcium release in mouse eggs. *Development (Cambridge)* **142**, 2633–2640 (2015).
89. Y. Jiang, M. Tian, W. Lin, X. Wang, X. Wang, Protein kinase serine/threonine kinase 24 positively regulates interleukin 17-induced inflammation by promoting IKK complex activation. *Front. Immunol.* **9**, 921 (2018).
90. J. Zhao, B. Wang, H. Yu, Y. Wang, X. Liu, Q. Zhang, tdrd1 is a germline-specific and sexually dimorphically expressed gene in Paralichthys olivaceus. *Gene* **673**, 61–69 (2018).
91. G. Hamamoto, T. Suzuki, M. G. Suzuki, F. Aoki, Regulation of transketolase like 1 gene expression in the murine one-cell stage embryos. *PLOS ONE* **9**, e82087 (2014).
92. K.-Y. Ryu, S. A. Sinnar, L. G. Reinholdt, S. Vaccari, S. Hall, M. A. Garcia, T. S. Zaitseva, D. M. Bouley, K. Boekelheide, M. A. Handel, M. Conti, R. R. Kopito, The mouse polyubiquitin gene Ubb is essential for meiotic progression. *Mol. Cell. Biol.* **28**, 1136–1146 (2008).
93. S. Maenohara, M. Unoki, H. Toh, H. Ohishi, J. Sharif, H. Koseki, H. Sasaki, Role of UHRF1 in de novo DNA methylation in oocytes and maintenance methylation in preimplantation embryos. *PLOS Genet.* **13**, e1007042 (2017).
94. X. Liu, Y. Wang, P. Zhu, J. Wang, J. Liu, N. Li, W. Wang, W. Zhang, C. Zhang, Y. Wang, X. Shen, F. Liu, Human follicular fluid proteome reveals association between overweight status and oocyte maturation abnormality. *Clin. Proteomics* **17**, 22 (2020).
95. Y. Rong, S. Y. Ji, Y. Z. Zhu, Y. W. Wu, L. Shen, H. Y. Fan, ZAR1 and ZAR2 are required for oocyte meiotic maturation by regulating the maternal transcriptome and mRNA translational activation. *Nucleic Acids Res.* **47**, 11387–11402 (2019).

Acknowledgments: We thank the members of the Shikanov, Li, and Hammoud laboratories for scientific discussions and manuscript feedback. We thank the Advanced Genomics and Flow Cytometry Core Facilities at the University of Michigan and their staff for guidance and assistance with sample processing and the Michigan Institute for Data Science and the Michigan Single-Cell Spatial Analysis Program for support. **Funding:** This work was supported by Chan Zuckerberg Foundation grant CZF2019-002428 (A.S., E.E.M., J.Z.L., and S.H.) and NIH grants R01-HD099402-03 (A.S. and J.Z.L.), F31-HD106626 (A.S.K.J.), T32-HD079342 (A.S.K.J.), T32-GM70449 (D.F.H.), and T32- GM141746 (D.F.H.). **Author contributions:** Conceptualization: A.S.K.J., D.F.H., J.Z.L., A.S., J.H.M., Q.M., N.D.U., and Y.S. Methodology: A.S.K.J., D.F.H., S.H., J.Z.L., and A.S. Sample collection and sequencing: A.S.K.J. and D.F.H. Histology: A.S.K.J., A.T., and M.C. Computational analysis: D.F.H. and J.Z.L. Supervision: J.Z.L., A.S., E.E.M., and S.H. Writing—original draft: A.S.K.J. Writing—review and editing: A.S.K.J., D.F.H., V.P., J.Z.L., and A.S. **Competing interests:** The authors declare that they have no competing interests. **Data and materials availability:** All data needed to evaluate the conclusions in the paper are present in the paper and/or the Supplementary Materials. Raw data for the two samples analyzed by NanoString and three samples analyzed by scRNA-seq are deposited in the Gene Expression Omnibus (GSE260685 and GSE260686).

Submitted 3 November 2023
Accepted 4 March 2024
Published 5 April 2024
10.1126/sciadv.adm7506